The thermal plumbing system of Stromboli volcano, Aeolian Islands (Italy) inferred from electrical conductivity and induced polarization tomography

André Revil, Anthony Finizola, Tim Johnson, Tullio Ricci, Marceau Gresse, Eric Delcher, Stéphanie Barde-Cabusson, Pierre-Allain Duvillard, Maurizio Ripepe

JGR Solid Earth

RESEARCH ARTICLE
10.1029/2023JB026475

Special Section:
Advances in understanding volcanic processes

The Thermal Plumbing System of Stromboli Volcano, Aeolian Islands (Italy) Inferred From Electrical Conductivity and Induced Polarization Tomography

A. Revil[1], A. Finizola[2,3], T. Johnson[4], T. Ricci[5], M. Gresse[6], E. Delcher[2,3], S. Barde-Cabusson[7], P. A. Duvillard[8], and M. Ripepe[9]

[1]CNRS, UMR CNRS 5204, EDYTEM, Université Grenoble Alpes, Univ. Savoie Mont-Blanc, Le Bourget du Lac, France, [2]Laboratoire GéoSciences Réunion, Université de La Réunion, Saint Denis, France, [3]CNRS, Institut de physique du globe de Paris, Université de Paris, Paris, France, [4]Pacific Northwest National Laboratory, Richland, WA, USA, [5]Istituto Nazionale di Geofisica e Vulcanologia, Roma, Italy, [6]Geological Survey of Japan, AIST, Research Institute of Earthquake and Volcano Geology, Tsukuba, Japan, [7]Naga Geophysics, Technolac, Le Bourget du Lac, France, [8]Styx4D, Technolac, Le Bourget du Lac, France, [9]Department of Earth Science, University of Florence, Firenze, Italy

Key Points:

- A 3D electrical conductivity tomography is performed at Stromboli volcano, Italy
- Chargeability data are also obtained along a profile crossing the volcano
- A temperature tomogram is obtained by combining the conductivity and induced polarization data

Correspondence to:
A. Revil,
andre.revil@univ-smb.fr

Citation:
Revil, A., Finizola, A., Johnson, T., Ricci, T., Gresse, M., Delcher, E., et al. (2023). The thermal plumbing system of Stromboli volcano, Aeolian Islands (Italy) inferred from electrical conductivity and induced polarization tomography. *Journal of Geophysical Research: Solid Earth*, *128*, e2023JB026475. https://doi.org/10.1029/2023JB026475

Received 28 JAN 2023
Accepted 6 JUN 2023

Author Contributions:
Conceptualization: A. Revil, A. Finizola, E. Delcher
Data curation: A. Revil, A. Finizola
Formal analysis: A. Revil, A. Finizola, T. Johnson, M. Gresse, E. Delcher, S. Barde-Cabusson, P. A. Duvillard
Funding acquisition: A. Revil, A. Finizola, T. Ricci
Investigation: A. Revil, A. Finizola, T. Johnson, T. Ricci, M. Gresse, E. Delcher, S. Barde-Cabusson, P. A. Duvillard, M. Ripepe
Methodology: A. Revil, A. Finizola, T. Johnson, T. Ricci, M. Gresse
Project Administration: A. Revil, A. Finizola, T. Ricci
Resources: A. Revil, A. Finizola

Abstract We performed the first 3D island-scale tomography of the electrical conductivity of Stromboli volcano (Aeolian Islands, Italy) using 2D acquisition lines (37.2 km) and a total of 18,880 measurements and 2,402 unique electrode locations. This 3D data set was inverted using a Gauss-Newton algorithm, parallel-processing on an unstructured tetrahedral mesh containing 678,420 finite-element nodes and 3,580,145 elements to account for the topography of the volcanic island. The tomogram exhibits a conductive body (10^{-2}–1.0 S m^{-1}) consistent with the location of CO_2 and temperature anomalies observed at the ground surface. It corresponds to the hydrothermal system with high electrical conductivity associated with alteration. In order to confirm this interpretation, a 2.5D large-scale induced polarization tomography was performed crossing the volcano. The joint interpretation of the conductivity and normalized chargeability is done with a petrophysical model previously tested and verified at both shield- and strato-volcanoes. This model implies that alteration (through the effect of the cation exchange capacity associated with clay minerals and zeolites) plays a strong role in both controlling the electrical conductivity and normalized chargeability at Stromboli volcano. A temperature tomogram, derived from the geoelectrical measurements, is consistent with surface temperature anomalies and the Very Long Period (VLP) seismicity related to the mild-explosive activity. This survey displays at 600 m a.s.l. a lateral shift in the highest temperature location, also corresponding to the source of VLP seismicity. Structural boundaries have a major role in the hottest hydrothermal fluids rising below the active crater terrace of Stromboli volcano.

Plain Language Summary Stratovolcanoes form unstable edifices responsible for pyroclastic flows and flank collapses. The mechanical weakening of a volcanic edifice can be connected to alteration processes. Alteration denotes the replacement of silicates by secondary mineral assemblages including aluminosilicates. Clay minerals influence the geoelectrical properties of a volcano. Recent studies have demonstrated that induced polarization can image alteration. The tomograms are used to delineate the position of the hydrothermal body of Stromboli and infer the temperature distribution inside the volcanic edifice.

1. Introduction

Stromboli Island is located in the northernmost of the Aeolian archipelago in the Southern Tyrrhenian Sea, Italy (Figure 1). The formation of the Aeolian Islands is related to the subduction of the African plate below the Eurasian plate (Barberi et al., 1974; Keller et al., 1993). Stromboli itself rises from a depth of 2,000 m below sea level to an elevation of 924 m a.s.l. (meters above sea level, see Romagnoli et al., 2009). The emerged part of the volcano developed during the last 100 ka (Rosi, 1980).

Stromboli is a permanently active and fairly accessible stratovolcano. It is considered a key natural laboratory for geophysical investigations aimed at better understanding its internal structure and structural control of its hydrothermal activity (Bonaccorso et al., 2003; Chouet et al., 2003; Revil et al., 2004). One of the first geophysical studies performed on Stromboli used land-based magnetic data to map magnetic anomalies related to the volcanic activity (Bossolasco, 1943, see also Casertano & Pinna, 1971; Yokoyama, 1959). Later on, aeromagnetic studies

Software: T. Johnson
Supervision: A. Revil, A. Finizola
Validation: A. Revil, A. Finizola, T. Johnson, T. Ricci, E. Delcher, S. Barde-Cabusson
Visualization: A. Revil, A. Finizola, M. Gresse, P. A. Duvillard
Writing – original draft: A. Revil, A. Finizola, T. Johnson
Writing – review & editing: A. Revil, A. Finizola, T. Ricci, M. Gresse, S. Barde-Cabusson, P. A. Duvillard, M. Ripepe

were carried out at a regional scale using airborne magnetic surveys (Azienda Generale Italiana Petroli in 1982, Okuma et al., 2003, 2009). Okuma et al. (2009) interpreted their observations in terms of past and recent activity and their preliminary 3-D tomogram of magnetization was used to constrain the geometry of some volcanic units. They identified a zone of demagnetization under the summit area, interpreted as rocks affected by hydrothermal activity and the thick accumulation of highly permeable pyroclastic rocks.

Bonasia et al. (1973) found a large negative gravity Bouguer anomaly in the central part of the volcanic edifice, although these results have been questioned by Linde et al. (2014) due of the absence of terrain or bathymetric corrections. A detailed land-based gravity survey was conducted by Linde et al. (2014) with a total of 543 gravity stations complemented with a subset of 327 sea-surface gravity data. This data set was inverted in 3D in terms of density distribution using a high-resolution digital elevation model (DEM) including the bathymetry around the island of Stromboli. This tomogram was interpreted in terms of geological structures and location of the hydrothermal plumbing system.

Recently, Patanè et al. (2017) realized a 3D seismic velocity model of the volcano down to a depth of 4 km by integrating the data of artificial and natural seismic sources recorded during a seismic tomography survey (Castellano et al., 2008). This study localized magma accumulation zones and the geometry of the shallow plumbing system. Tioukov et al. (2019) used muon absorption radiography to image the internal structure of the crater area. Their data were used to depict the collapse structure associated with the 2003 and 2007 eruptions. Finally, Calò et al. (2021) used 4 years of ambient seismic noise data (2010–2013) to reconstruct the shallow 4D seismic velocity tomogram of the volcanic edifice and characterize the location of its hydrothermal body.

In the past 20 years, geoelectrical studies have also contributed to gathering valuable structural information in key areas of Stromboli. For instance, Finizola et al. (2003) mapped the extent of the hydrothermal activity in the Fossa, that is, the summit area, using a combination of self-potential, ground temperature, and CO_2 concentration measurements. Electrical conductivity tomography is a galvanometric technique imaging the low-frequency (~1 Hz) electrical conductivity/resistivity (for volcanoes see for instance Johnson et al., 2010; Linde & Revil, 2007; Soueid Ahmed et al., 2018, and references therein). An electrical current is injected and retrieved between two (current) electrodes and the resulting electrical field (or one of its components) is measured between other (voltage) electrodes. These data are then inverted to obtain a tomogram of the electrical conductivity/resistivity distribution of the volcano (Johnson et al., 2010; Revil et al., 2010). Revil et al. (2004) performed an electrical resistivity survey in the Fossa of Stromboli in addition to additional self-potential, ground temperature, and soil CO_2 concentration data. Self-potential data provides a non-intrusive ground water flow sensor through the electrokinetic coupling effect (Hermans et al., 2014; Jardani et al., 2009; Revil & Pezard, 1998; Titov et al., 2005). They showed the presence of a shallow perched aquifer standing above the hydrothermal plumbing system that is close enough to the active volcanic vents to present a risk. Repetitive measurements of self-potential, CO_2 concentration, and temperature data crossing La Fossa were performed during the 2002–2003 Stromboli eruptive crisis (Finizola et al., 2009). These data demonstrated the role of the structural heritage of the volcano in the hydrothermal fluid preferential flows during an unrest period.

Further larger scale electrical resistivity surveys provided geological, structural, and hydrogeological information to a depth of 200 to ~500 m (Carapezza et al., 2009; Finizola et al., 2006, 2010; Revil et al., 2011). In particular, Revil et al. (2011) used an extended data set composed of large-scale electrical resistivity tomography, self-potential, soil temperature, and soil CO_2 concentration and flux data to study the hydrothermal system and hydrogeology at the scale of the emerged part of Stromboli. Based on those results, the authors proposed interpretations for a greater extension of the hydrothermal system than previously thought and for the presence of perched aquifers. Revil et al. (2011) imaged the major structures of the volcano such as the gas-impermeable structure of NeoStromboli crater or the Rina Grande degassing sector collapse.

The conductivity of rocks is sensitive to the water content and salinity of the pore water, temperature and pH, as well as alteration (due to the cation exchange capacity of clays and zeolites, see Soueid Ahmed et al., 2018). It is therefore a powerful and suitable technique to localize hydrothermal systems (Komori et al., 2010; Revil, Ghorbani, et al., 2018, Revil, Qi, et al., 2018; Richards et al., 2010). It can be also used to image geohazards associated with slope instabilities and the presence of shallow aquifers in the vicinity of active volcanic vents (e.g., Gonzales et al., 2014). Unfortunately, electrical conductivity is sensitive to too many parameters to be easily interpretable as a stand-alone technique, especially in volcanic systems (Soueid Ahmed et al., 2018). Consequently, it is often used as a qualitative method. This fact is often overlooked in the literature and is therefore responsible

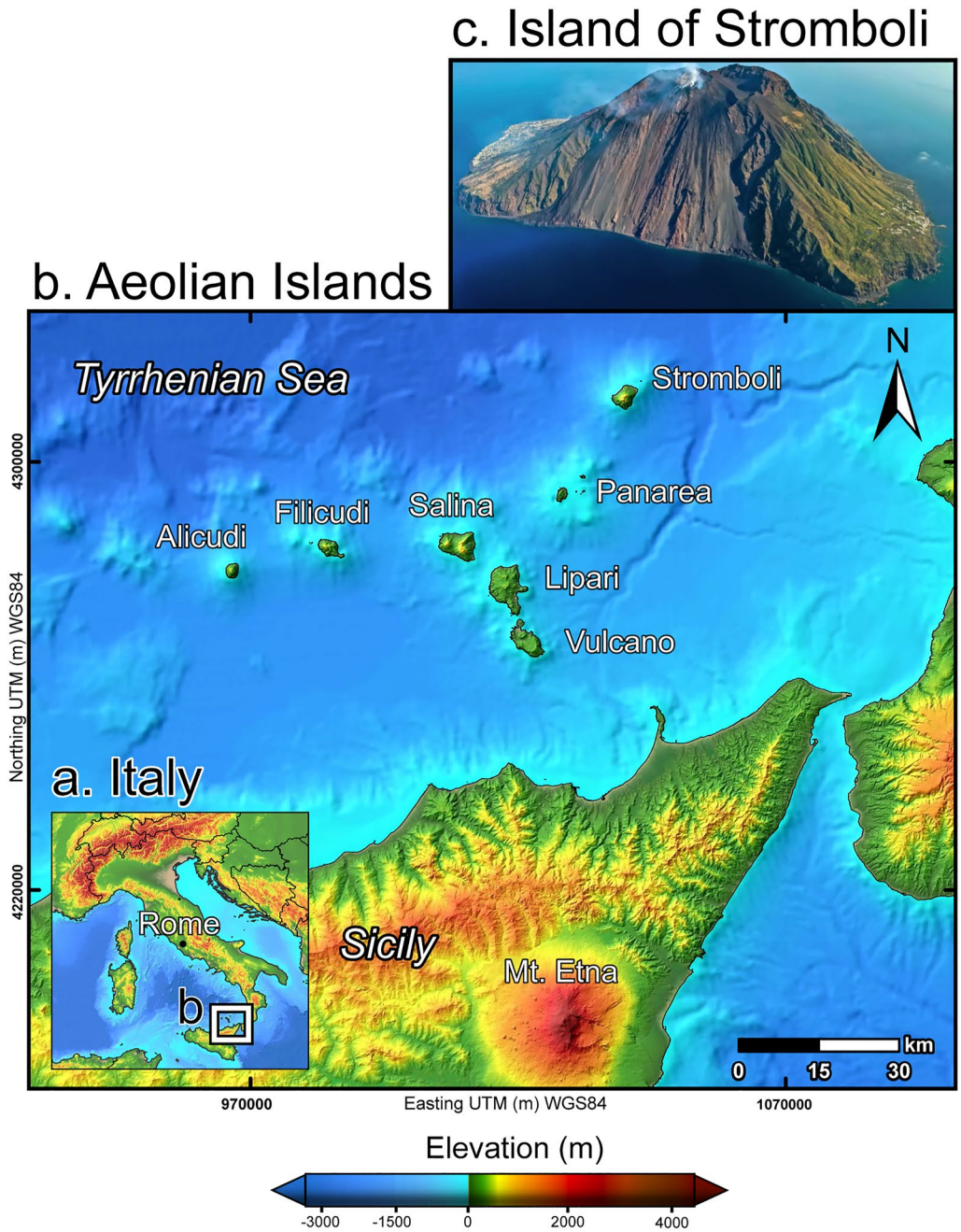

Figure 1. Stromboli Island. (a) Position of the Aeolian Islands in the Tyrrhenian Sea (insert). (b) The Aeolian archipelago is located in the vicinity of the Northern coast of Sicily. It is composed of seven main islands (Alicudi, Filicudi, Salina, Lipari, Panarea, Stromboli, and Vulcano). (c) Picture showing the island of Stromboli. The map was created using Esri ArcGIS 10.8 software (see http://www.esri.com) with the free digital elevation models: TINITALY DEM (Tarquini et al., 2007) and GEBCO 2021 Gridded Bathymetry Data (https://download.gebco.net/).

for the over-interpretation of resistivity/conductivity tomograms using inadequate petrophysical models ignoring surface conductivity associated with alteration.

A complementary technique to conductivity tomography is induced polarization, which is able to image an additional petrophysical property called normalized chargeability (e.g., Revil & Gresse, 2021). Induced polarization can be performed with the same equipment as electrical conductivity. The electrical conductivity of rocks characterizes their ability to conduct an electrical current under a given (applied) electrical field. The normalized

chargeability of rocks reflects their ability to store reversibly electrical charges (Olhoeft, 1983, 1985). In recent studies, a petrophysical model has been developed to jointly interpret electrical conductivity and normalized chargeability data (Revil, Ghorbani, et al., 2018; Revil, Qi, et al., 2018, and references therein) and to decipher the position of hydrothermal bodies (Revil & Gresse, 2021).

In the present paper, we provide the first 3D conductivity tomogram of Stromboli volcano down to the sea level. The resistivity/conductivity measurements were performed at various scales including with an unusually long cable (2.52 km in length and spacing between the electrodes of 40 m). The 3D tomogram is interpreted with an additional induced polarization survey performed along a section crossing the volcano. By combining both the electrical conductivity and normalized chargeability data, we assess the importance of alteration on these electrical properties, and we obtain the first temperature tomogram of the volcano. Different cross-sections of temperature tomogram crossing the active crater area are compared to additional data including seismicity (volcano-tectonic and Very Long Period (VLP) signals), soil CO_2 concentrations, self-potential and shallow temperature data.

2. Stromboli Island

2.1. Geological Structure

We first present an up-to-date interpretation of the structural geology of the aerial edifice of Stromboli. The emerged volcanic edifice, built up during the last 100 ka, can be divided into six main episodes, each separated by erosional deposits and/or by caldera formation and/or lateral flank collapse (Francalanci et al., 2013; Hornig-Kjarsgaard et al., 1993; Keller et al., 1993; Pasquarè et al., 1993; Rosi, 1980): PaleoStromboli I (PST I), PaleoStromboli II (PST II), PaleoStromboli III (PST III), Vancori period, Neostromboli and Recent Sciara. The southern and eastern aerial flanks of Stromboli have been affected by the two oldest collapses cutting the PaleoStromboli Units, respectively at the end of PST II and PST III period (see lateral collapse rim cutting the coastline in Figure 2). During the PaleoStromboli period, a succession of four caldera collapses occurred. Three of them were associated with the end of PST I (~67 ka), PST II (~54 ka), and PST III (~34 ka) period (see label "PST I," "PST II," "PST III" in Figure 2). The fourth one in this period is located between Lower PST III and Upper PST III Unit.

The three last periods began 26 ka ago. They are first defined by the last caldera collapse separating the Lower from the Middle Vancori Units. The Vancori period finished 13 ka ago by the largest and oldest lateral collapse oriented toward the Northwestern direction (Sciara del Fuoco). The following period, NeoStromboli (13–4 ka ago), was characterized by two other nested lateral collapse structures identified in the Easternmost Sciara del Fuoco area and structuring also the Fossetta area. The last period called Recent Sciara is first characterized by a lateral sector collapse toward the East (Rina Grande) cutting the second summit of the island, Pizzo, followed by a lateral sector collapse toward the Northwest cutting the Fossa area and inside which are located the present day SW, C (Central) and NE active craters.

Finally, two major faults, namely the N41°- and N64°-faults, were evidenced thanks to anomalous CO_2 degassing and mofette areas located in Piscità-San Bartolo and Pizzillo area (Carapezza et al., 2009; Finizola et al., 2002).

2.2. Soil Temperature Anomalies

A total of 5,720 soil temperatures measurements (performed at a depth of 30 cm) were acquired between 1995 and 2012 following the protocol described by Finizola et al. (2003). A probability plot technique analysis (Sinclair, 1974) was applied on all the temperature measurements in order to evidence thresholds in the mode of heat transfer. Two inflexion points were identified at 52.4 and at 31.7°C, separating two areas mainly governed respectively by convective and conductive heat transfer (Figure 3a). These thresholds were used to define the color scale for Figures 3b and 3c. Except for a circumscribed vapor emission due to the impact of a ballistic block (see "BIC", Block Impact Crater—in Figure 3b present on the Northeast flank of the volcano, Finizola et al., 2010), all the significant temperature anomalies are located in the summit area of the volcano (Finizola et al., 2002). The detailed summit temperature map displays anomalies located close to the Pizzo area (see "P1," "P2," and "P3" in Figure 3c; Finizola et al., 2003). Their distribution is influenced by the gliding plane of Rina Grande lateral collapse. Other anomalies are located in the Fossa area. They correspond to the active crater terrace. In this sector, "F2" and "F5" anomalies are related to the position of the SW- and NE-crater respectively.

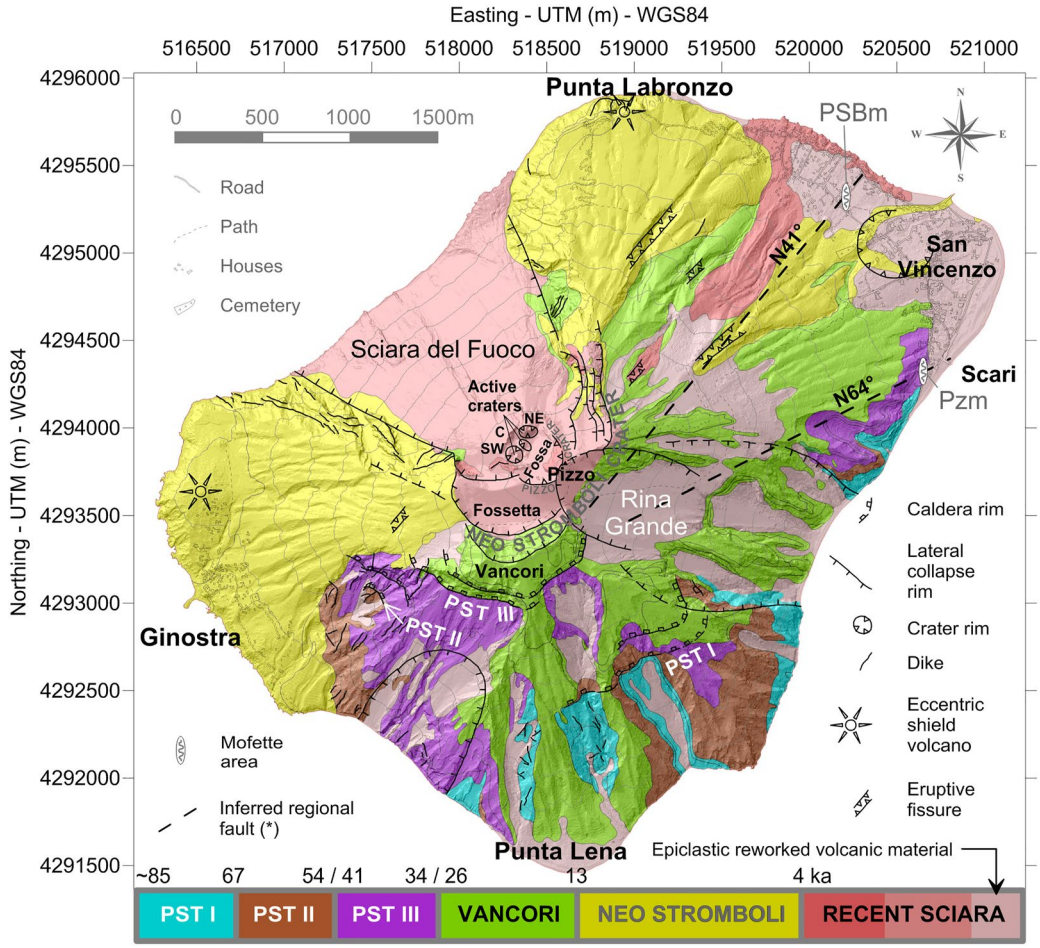

Figure 2. Geological map of the island of Stromboli. We used the maps produced by both Keller et al. (1993), Francalanci (1987), and Francalanci et al. (2013) with additional structural information regarding the regional faults from Finizola et al. (2002).

The "F1," "F3," "F4," and "F6" anomalies are associated with the fault system of an old hidden crater rim located inside the Fossa area (see Figure 3c and discussions in Finizola et al., 2003, 2009).

2.3. Thermal Infrared Satellite Data

The Stromboli surface temperature (Figure 3d) was also recovered using remote sensing satellite. Landsat-8 data were collected using the USGS Earth Explorer portal (https://earthexplorer.usgs.gov). The thermal image of the volcano was retrieved using the closest night time and cloud-free scene to the resistivity surveys, corresponding to 4 December 2013, 20:47 UTC (see Appendix A for details). The recovered temperature map is consistent with the subsurface temperature map, and reflects the main anomalies of the active vents, with maximum values reaching 792°C.

2.4. Soil CO_2 Concentration Anomalies

A total of 3,582 soil CO_2 concentration measurements at depth of about 0.5 m were acquired between 1995 and 2012 with the same protocol described by Finizola et al. (2006). Although the measurements were acquired in different periods, the high range of fluctuation for CO_2 concentration anomalies (few orders of magnitude) allows evidencing, without doubt, the different anomalies. Moreover, the CO_2 concentration data set used in this survey, instead of the CO_2 flux from the soil, permits us to reduce CO_2 flux anomalies potentially generated during strong wind days by Venturi effect (Carapezza et al., 2009). Repeated measurement along the same CO_2 concentration profiles, performed in different periods, always display the same location for CO_2 anomalies (see for instance the Ginostra-Scari profile in Finizola et al., 2006; Revil et al., 2011).

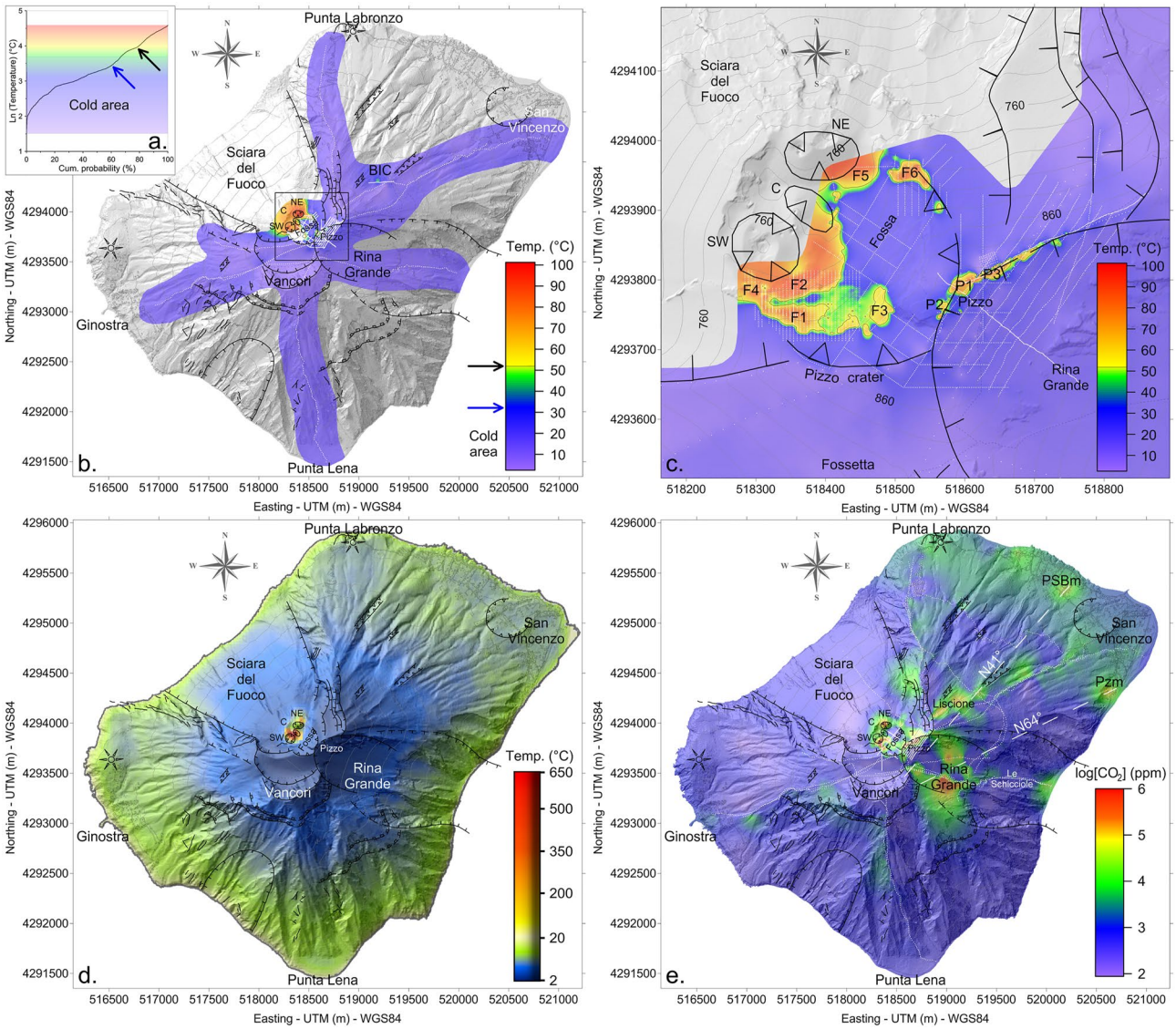

Figure 3. Stromboli surface temperature and diffuse degassing. The white dots in figure (b–e) correspond to the temperature and diffuse degassing measurements. (a) Probability plot analysis (Sinclair, 1974) on temperature data measured at 30 cm depth evidencing two inflexion points; at 31.7 (blue arrow) and 52.4°C (black arrow). (b) Temperature map at 30 cm depth with the probability plot results included into the color scale (color transition in correspondence with the blue and black arrows). The black rectangle evidence the detailed area shown in (c). (c) Detailed temperature map at 30 cm depth of the summit area with the probability plot results included in the color scale (modified from Finizola et al., 2003). (d) Land surface temperature obtained from dual-band technique using Landsat-8 night-time images of 4 December 2013. The hot surface temperature area T_h (>20°C) only appears around the main vents due to the presence of both Short-Wave Infrared (SWIR) and long-wave infrared (TIR) components. In other areas, the SWIR band component is null, and the surface temperature corresponds to the TIR band (see Appendix A). (e) Soil carbon dioxide concentration map measured at 50 cm depth (modified from Finizola et al., 2002). Other symbols: same as Figure 2.

The CO_2 anomalies located in the summit area agree with the position of the thermal anomalies (see respectively Figures 3e and 3c). At lower altitudes, the CO_2 peaks evidence the position of two regional faults with N41° and N64° orientations (Finizola et al., 2002). These faults cross the seashore at the mofette area of Piscità—San Bartolo (see "PSBm" in Figure 3e) and at the mofette area of Pizzillo ("Pzm" in Figure 3e), respectively.

2.5. Self-Potential Anomalies

A total of 8,927 self-potential data were acquired between 1995 and 2012 with the same protocol described by Finizola et al. (2002). All the profiles were corrected with loop correction as shown in Barde-Cabusson et al. (2021). The zero potential was taken at the sea. The corresponding self-potential map (Figure 4) has been

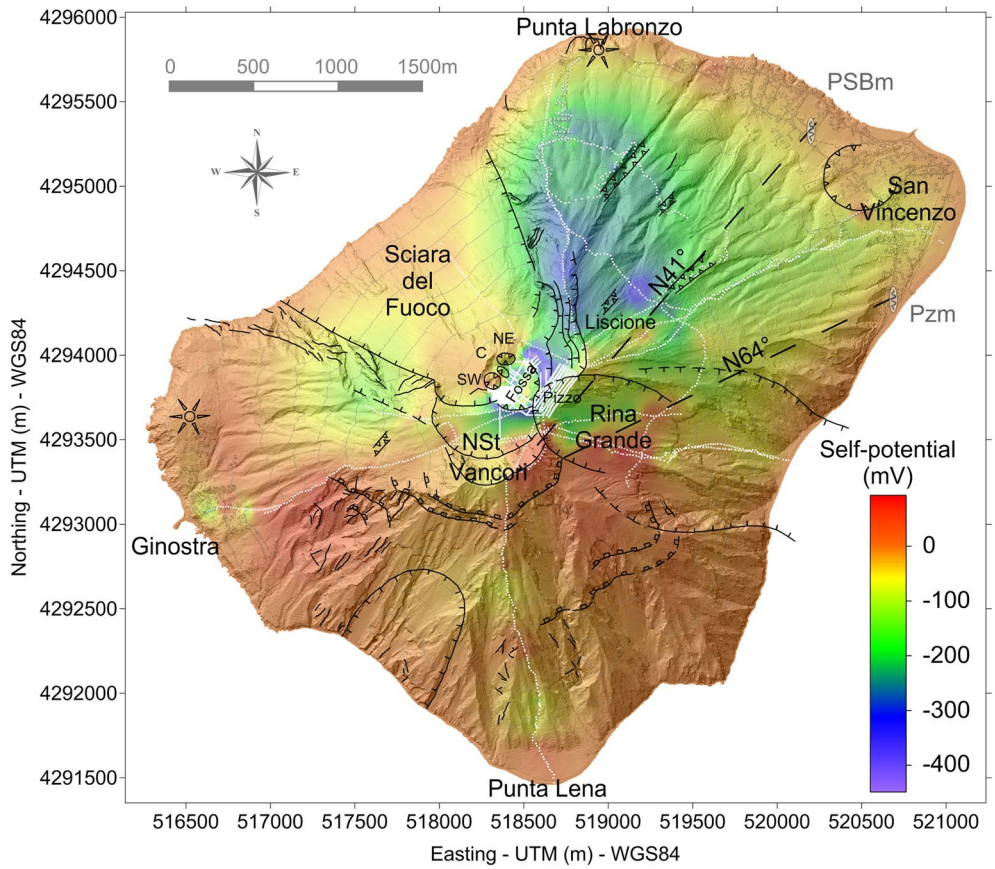

Figure 4. Self-potential (SP) map of Stromboli volcano (modified from Finizola et al., 2002, 2003). The SP map reflects self-potential anomalies of electrokinetic nature associated with ground water flow pattern at the scale of the volcano. Positive anomalies are typical of the upflow of water while negative anomalies may represent the signature of downward flow (see Revil et al., 2010, for Vulcano in the Aeolian Islands, Italy). "NSt" stands for NeoStromboli crater rim. Other symbols: same as Figure 2.

obtained using the two steps interpolation method proposed by Barde-Cabusson et al. (2021). As described by Finizola et al. (2003) and Revil et al. (2004), the self-potential map displays higher self-potential anomalies in the Fossa and Pizzo areas co-localized with temperature and CO_2 concentration anomalies. In the lower part of the edifice, the self-potential map does not fit with a simple hydrothermal/hydrogeological model, as described on other volcanoes (Izu-Oshima volcano, Ishido, 2004; Misti volcano, Finizola et al., 2004; Ubinas volcano, Gonzales et al., 2014, or El Teide volcano, Villasante-Marcos et al., 2014, Miyakejima volcano, Gresse et al., 2021). In the upper part of the edifice, this map evidences electrokinetic anomalies associated with ground water flow, especially preferential ground water flow pathways, through the streaming current mechanism (e.g., Bolève et al., 2011; Revil et al., 2005). The positive anomalies are associated with rising hydrothermal fluids and hydromechanical disturbances that can generate transient self-potential anomalies (Revil et al., 2003). In the lower part of the edifice, the groundwater flows down along structural boundaries generating negative self-potential anomalies (see Finizola et al., 2002, 2010; Revil et al., 2011).

3. Electrical Conductivity Tomography

3.1. Description of the Survey

A total of 18,879 electrical conductivity measurements have been acquired on Stromboli volcano through eight surveys performed between 2002 and 2012 (37.2 km of profiles in total). Thirty profiles were performed, and only six of them have been published to date in the form of cross-sections with a 2.5D inversion algorithm (Finizola et al., 2006, 2010; Revil et al., 2004, 2011; see Table 1).

Table 1
Summary of the Resistivity and Induced Polarization Profiles Performed at Stromboli Volcano

ID	Year	Spacing (m)	Area investigated	Length (m)	*N*	Reference
1	2002	5	Fossa-N-S	315	507	R2004; F2009
2	2004	20	Ginostra-Scari	3,820	1,841	F2006
3	2005	20	500 m a.s.l.	2,220	1,207	U
4	2005	20	250 m a.s.l.	2,340	1,201	U
5	2005	20	Rina Grande-Fossetta	1,260	391	U
6	2005	20	Old-Touristic-path	1,240	426	U
7	2006	5	Pizzo-Helicopter pad-1	315	425	U
8	2006	5	Pizzo-Helicopter pad-2	315	422	U
9	2006	5	Pizzo-Helicopter pad-3	315	426	U
10	2006	5	Pizzo-Helicopter pad-4	315	426	U
11	2006	5	Pizzo-Helicopter pad-5	315	424	U
12	2006	5	Pizzo-Helicopter pad-6	315	381	U
13	2006	5	Pizzo-Helicopter pad-7	315	387	U
14	2006	5	Pizzo-Helicopter pad-8	315	412	U
15	2008	5	Nel Cannestrà	315	452	F2010
16	2008	5	Pizzillo	315	401	U
17	2008	5	Pizzo-Helicopter pad	315	472	U
18	2008	5	Pizzo-Rina Grande	315	472	U
19	2008	5	Sciara del Fuoco-Rina Grande	315	472	U
20	2009	5	Nel Cannestrà-BIC-1	315	362	U
21	2009	5	Nel Cannestrà-BIC-2	315	342	U
22	2009	5	Nel Cannestrà-BIC-3	315	427	U
23	2009	5	Nel Cannestrà-BIC-4	315	446	U
24	2009	5	Nel Cannestrà-BIC-5	315	447	U
25	2009	5	Direttissima	635	1,099	F2010
26	2011	40	Ginostra-Le Schicciole	3,640	737	R2011
27	2011	40	Ginostra-Scari	5,080	1,055	R2011
28	2012	40	Circum-Sciara del Fuoco	3,480	744	U
29	2012	40	Punta Labronzo-Punta Lena	5,000	1,195	U
30	2012	40	Circum-Sciara del Fuoco-DD	2,520	880	U

Note. N denotes the total number of measurements of each profile (30 profiles in total). All profiles are done using a Wenner-alpha array except profile 30, which is a dipole-dipole configuration. R2004 and R2011 corresponds to Revil et al. (2004, 2011), respectively, F2006, F2009, and F2010 to Finizola et al. (2006, 2009, 2010) respectively, and U corresponds to unpublished. The total length of the profiles is 37,220 m for 18,879 measurements.

Electrical conductivity measurements were obtained using a set of 64 stainless steel and brass electrodes. We use an ABEM Terrameter SAS-4000 impedance meter for these surveys. The electrode spacing was 5, 20, and 40 m depending on the profiles (Table 1). All the profiles with an electrode spacing of 5 and 20 m spacing were performed in spring (May). The profiles with an electrode spacing of 40 m were performed in winter (December and January) to take advantage of the higher soil moisture responsible for lower contact resistances between the electrodes and the ground. For most of the surveys, the contact of the electrodes with the ground was further improved by adding a salty bentonite mud. The contact resistances were always below 3 kOhm as a result of such approach. The duration of the current injection was comprised between 0.5 and 1 s for all the surveys.

Most of the profiles were acquired with the Wenner array since it is characterized by a good signal-to-noise ratio. The profile with 40 m spacing between the electrodes (Table 1) located all around the Sciara del Fuoco collapse area was also acquired with dipole-dipole configuration in order to study the resistivity structure of the active

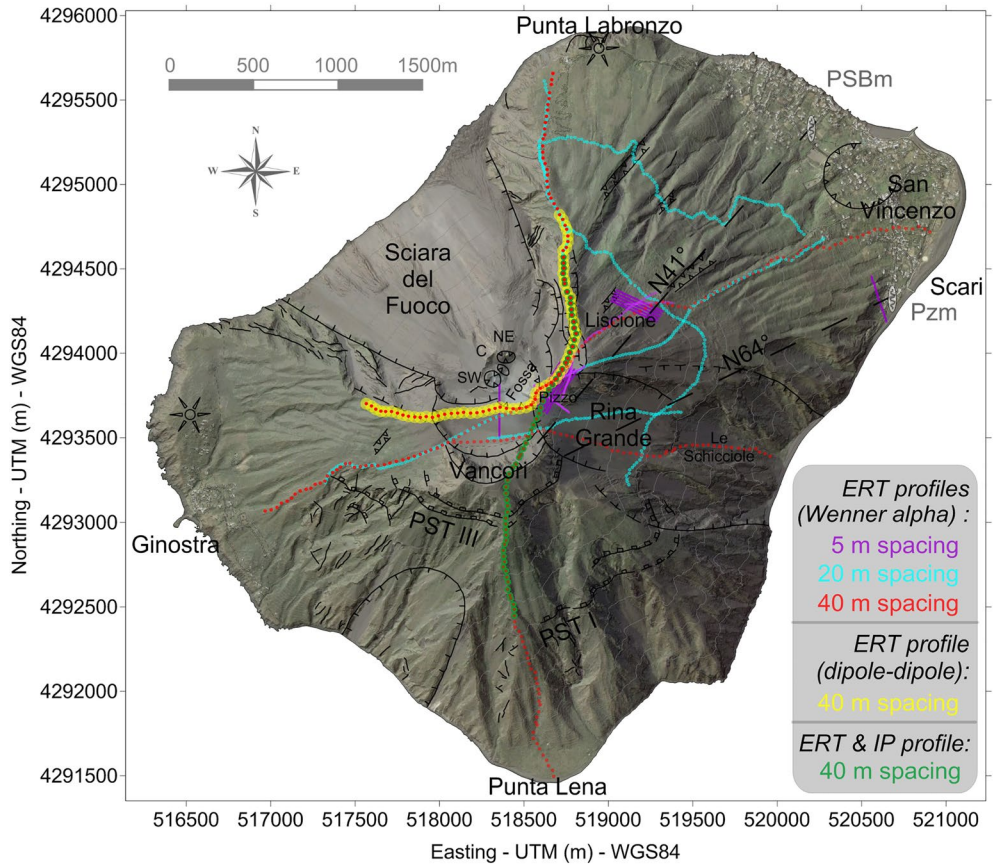

Figure 5. Position of the profiles used for the resistivity tomography and location of the IP profile. The acquisitions are done with spacing between the electrodes of 5, 20, and 40 m. The information on each profile is specified in Table 1. The green dots correspond to the IP profile commented in Figures 9 and 13. Other symbols: same as Figure 2.

crater area (see yellow profile in Figure 5). A profile with 40 m spacing crossing close to the Pizzo was acquired with induced polarization (green profile in Figure 5). Topography was extracted from the DEM of Marsella et al. (2012) with a mesh of 1 × 1 m, and a precision of 0.2 m in elevation. The horizontal coordinates were determined in the field using a GPS (Global Positioning System) with a precision of 3 m.

3.2. Forward and Inverse Modeling of the Conductivity Data

We use a forward modeling code to solve the classical elliptic equation for the electrical potential using a distribution of electrical conductivity and neglecting anisotropic effects (conductivity is considered as a scalar). The forward solved is based on the finite element technique (see Rücker et al., 2006; Soueid Ahmed et al., 2018, for details). The potential distribution for a single electrode used as a current source is first numerically obtained. Then, the potential distribution for a bipole AB (forming a source/sink current pair) is then built using the superposition principle. The 3D inversion is implemented into a parallel environment using 360 processors of a distributed memory supercomputer located at the Pacific Northwest National Laboratory, Richland WA, USA (see Johnson et al., 2010, for details).

We invert the apparent resistivity data by minimizing a cost function composed of a data misfit term and a model regularization term. We use a data covariance matrix to weight the data based on the error and the L_2 norm is used for the two terms. We use an Occam's type inversion scheme (the Occam inversion seeks the smoothest model among the models that fits the data to within an expected tolerance, see Constable et al., 1987). The resulting conductivity model results from a trade-off honoring the weighted resistivity data, which imposes heterogeneity, and the regularization constraint, which imposes homogeneity. The relative importance between the two terms of the cost function is controlled by the value of the regularization parameter. We use a cooling approach to deal

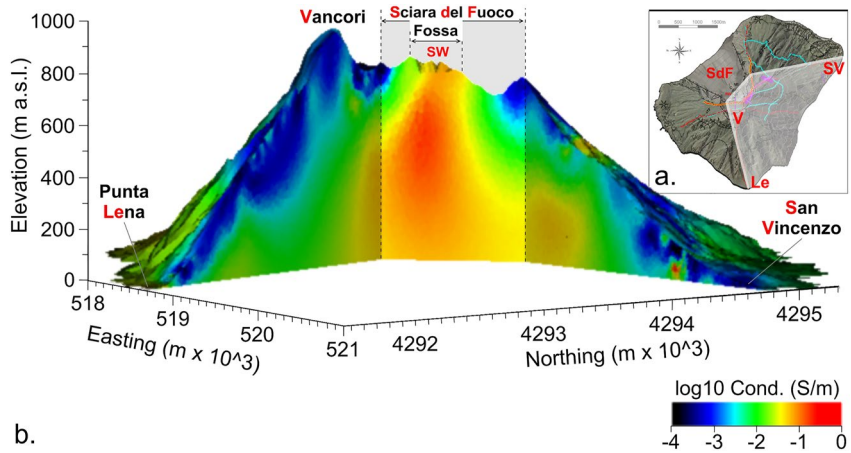

Figure 6. Electrical conductivity tomogram showing the variations of the electrical conductivity over four orders of magnitude from 1 to 10^{-4} S m^{-1}. (a) Position of the section crossing the Island of Stromboli. Le stands for Punta Lena, V for Vancori, SdF for Sciara del Fuoco and SV for San Vincenzo. (b) Cross-section of the electrical conductivity (in log-scale) obtained from the 3D conductivity tomogram.

with the value of this parameter during the inversion process: the trade-off parameter is initially set to a large value thereby imposing homogeneity in the inverse solution and then decreased as the algorithm progresses to allow sufficient heterogeneity to honor the weighted apparent resistivity data. In this way, the heterogeneity displayed in the final conductivity model is that which the apparent resistivity data are able to resolve. The objective function is minimized with the parallelized Conjugate Gradient Least Squares (CGLS) approach discussed by Johnson et al. (2010).

The topography of the emerged part of Stromboli is used to build the mesh for the forward and inverse models. In order to avoid edge effects, the Digital Elevation Map (DEM)-based topography was extrapolated outside the coast of the island. The resistivity survey utilized 2,402 unique electrode locations to collect 18,879 measurements used in the inversion. The computational mesh consists of ~678,000 finite-element nodes and ~3,580,000 tetrahedral elements. The large number of model elements is needed to precisely account for the rough topography of Stromboli and discretize the subsurface accordingly and according to the position of the electrodes where the mesh is refined. We point out, however, that the conductivity model resolution is not a function of the number of elements but depends instead on the information provided by the apparent resistivity data.

The computations required 6 hr and convergence was reached with 27 G-Newton iterations. Convergence is reached based on the level of data error: when the L_2 norm of the data misfit reduces to a value consistent with the estimated data noise level, the inverse solution is assumed to have converged to the right solution (Root Mean Square (RMS) error of 23% at the fifth iteration). The inverted conductivities typically range from 0.05 S m^{-1} to 3×10^{-4} S m^{-1} (Figures 6 and 7). At Stromboli, a conductivity of 0.05 S m^{-1} (~15 Ω m) is typical of the hydrothermal system (Finizola et al., 2006; Revil et al., 2004). A conductivity value of 3×10^{-4} S m^{-1} (3,000 Ω m) is typical of the fresh Vancori basalt unit or older Units (see position in Figure 2). However, as expressed above, electrical conductivity is not a direct lithological indicator and interpretation of the conductivity tomogram should be performed with care using petrophysical models validated on a broad range of experimental data. This point is further discussed in the next section.

3.3. Electrical Conductivity: Petrophysical Model

The electrical conductivity of a volcanic isotropic material is given by (e.g., Revil, Coperey, et al., 2017; Soueid Ahmed et al., 2018),

$$\sigma(\theta, T) = \frac{{s_w}^n}{F}\sigma_w(T) + \sigma_S(\theta, T), \quad (1)$$

$$\sigma(\theta, T) \approx \theta^m \sigma_w(T) + \sigma_S(\theta, T), \quad (2)$$

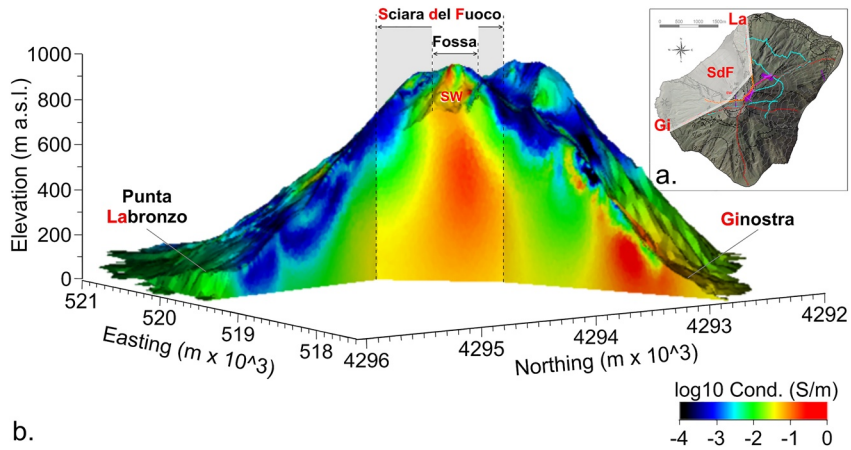

Figure 7. Electrical conductivity tomogram showing the variations of the electrical conductivity over four orders of magnitude. (a) Position of the section crossing the Island of Stromboli. Gi stands for Ginostra, SdF for the Sciara del Fuoco, and La for Punta Labronzo. (b) Cross-section of the electrical conductivity (in log-scale) obtained from the 3D conductivity tomogram.

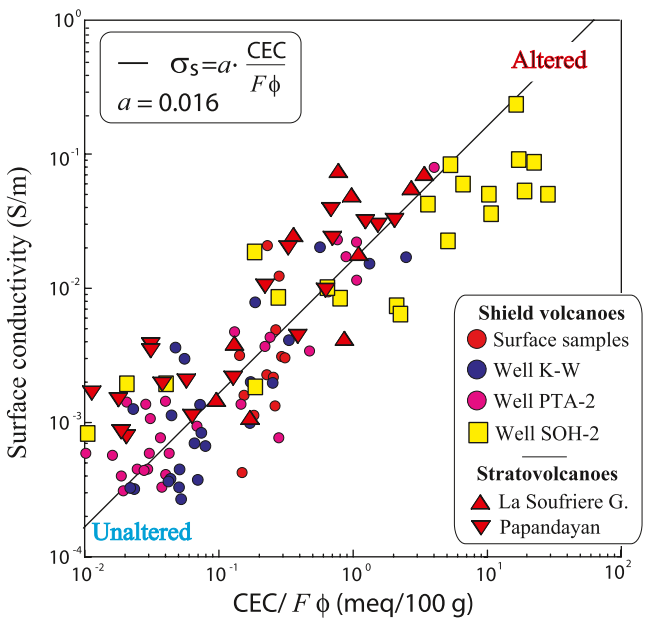

Figure 8. Results of the petrophysical investigations for the surface conductivity using volcanic rocks from both shield volcanoes and stratovolcanoes (Soufrière G. denotes the Soufrière of Guadeloupe volcano, Lesser Antilles, France). The surface conductivity (S m^{-1}) versus the reduced (or normalized) CEC defined as CEC/$F\phi$ where CEC denotes the cation exchange capacity (expressed here in meq/100 g), F the formation factor, and ϕ the connected porosity (1 meq/(100 g) = 963.2 C kg^{-1}). There are 93 samples in total. This trend is independent of the presence of metallic conductors in the mixture. According to our model, the slope is equal to $B\rho_g$. Keeping in mind that the CEC is here expressed in meq/100 g, using B (Na^+, 25°C) = 3.1 × 10^{-9} m^2 s^{-1} V^{-1} (effective mobility of the counterions in the electrical double layer coating the grains) and ρ_g = 2,900 kg m^{-3} (grain density) we have a = 0.012 S m^{-1} (meq/100g)$^{-1}$ close to the observed trend a = 0.016 ± 0.008 S m^{-1} (meq/100g)$^{-1}$ using the units for the conductivity and CEC used in the plot.

where σ_w (in S m^{-1}) corresponds to conductivity of the pore water, which depends on the salinity and temperature. In Equations 1 and 2, $0 \le s_w \le 1$ (dimensionless) denotes the water saturation (dry to saturated), $\theta = \phi s_w$ (dimensionless) denotes the volumetric water content, ϕ is the (connected) porosity, $m \ge 1$ (dimensionless) is called the porosity exponent or first Archie's exponent (Archie, 1942), $n \ge 1$ (dimensionless) is called the saturation exponent or second Archie's exponent (Archie, 1942), and σ_S (S m^{-1}) is called the surface conductivity (Revil & Glover, 1998; Waxman & Smits, 1968). To go from Equation 1 to Equation 2, we have assumed that the porosity and saturation exponents are the same that is, $m \approx n$ (see Revil, 2013, his Figure 18, for the case of sedimentary materials).

Surface conductivity characterizes conduction in the electrical double layer coating the solid (grain)/pore water interface (Revil et al., 2002; Waxman & Smits, 1968). An expression of the surface conductivity is given by Soueid Ahmed et al. (2018) and Revil et al. (2017a, 2017b)

$$\sigma_S(\phi, T) = \frac{s_w^{n-1}}{F\phi}\rho_g B\mathrm{CEC}, \quad (3)$$

$$\sigma_S(\theta, T) \approx \theta^{m-1}\rho_g B\mathrm{CEC}, \quad (4)$$

in saturated and unsaturated conditions, respectively. The quantity B (in m^2 V^{-1} s^{-1}) is the apparent mobility of the counterions in the electrical double layer coating the surface of the grains (Waxman & Smits, 1968), ρ_g denotes the grain density (in kg m^{-3}, typically ρ_g = 3,000 ± 200 kg m^{-3} for volcanic rocks), and CEC denotes the cation exchange capacity (in C kg^{-1}, 1 meq g^{-1} = 1 mol kg^{-1} = 96,320 C kg^{-1}). At saturation, $\theta^{m-1} = 1/F\phi$ where F (dimensionless) denotes the formation factor and ϕ (dimensionless) the connected porosity. The CEC is a rough proxy of the alteration of volcanic rocks when is associated with the formation of clays and zeolites resulting from the alteration of volcanic glasses (Revil et al., 2002). We have $\sigma_S = a\mathrm{CEC}\theta^{m-1}$ with $a = \rho_g B$ = 1.24 × 10^{-5} kg m^{-1} s^{-1} V^{-1} at 25°C (see Figure 8). Figure 8 demonstrates that the surface conductivity at room temperature and at saturation is controlled by the ratio of the cation exchange capacity and the tortuosity of the pore space (see Equation 3). The tortuosity of the pore space is defibed as the product of the formation factor by the (connected) porosity.

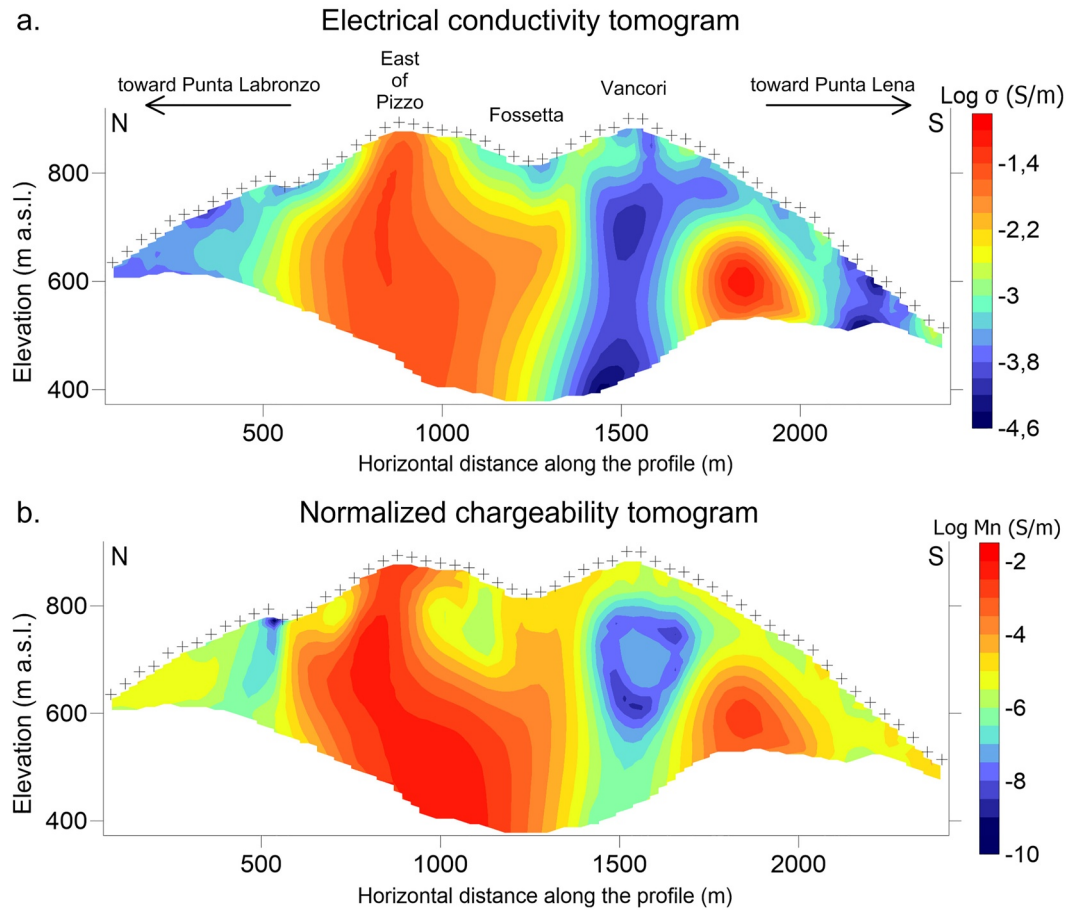

Figure 9. Large-scale 2.5D tomogram of the electrical conductivity σ and normalized chargeability M_n along a profile crossing the top part of Stromboli (view is from the Sciara del Fuoco, see green dots on Figure 5). A total of 708 data were inverted for both electrical conductivity and chargeability tomography. After 5 iterations, the Root Mean Square error is 23% for the electrical conductivity data and 5.0% for the chargeability data. The high values on both the conductivity and normalized chargeability tomograms are associated with alteration (especially the high CEC of the altered volcanic rocks with the presence of smectite).

In addition, electrical conductivity directly depends on temperature according to $\sigma_w(T) = \sigma_w(T_0)(1 + \alpha_w(T - T_0))$ for the pore water conductivity and $\sigma_S(T) = \sigma_S(T_0)(1 + \alpha_S(T-T_0))$, ($T_0 = 25$°C) (reference temperature), T denotes the ambient temperature of the solution, and $\alpha_w \approx \alpha_S \approx 0.02$/°C (Vinegar & Waxman, 1984). This temperature dependence is valid up to 200°C. As discussed below, there is another temperature dependence associated with the alteration itself.

4. Induced Polarization Tomography

4.1. Survey and Inversion

The induced polarization survey was acquired in 2012 with a 2.52 km profile and a spacing between the electrodes of 40 m. A total of 64 stainless steel electrodes were used for the survey. The duration of the current injection was set up to 1 s to polarize the volcanic rocks. For the secondary voltage measurements, we used a dead time of 0.1 s and a single window with a duration of 0.5 s. A total of 856 measurements were taken and 708 data were inverted for both electrical conductivity and chargeability tomography. The apparent chargeability was obtained by integrating the secondary voltage in the time window 0.1–0.6 s and normalizing the result by the product of the voltage just before shutting down the primary current and the duration of the time window (500 ms).

The position of the profile is shown in Figure 5 (green profile). This is a nearly North-South profile with the direction Punta Labronzo—Punta Lena, crossing both Vancori and the Eastern side of Pizzo. The inversion

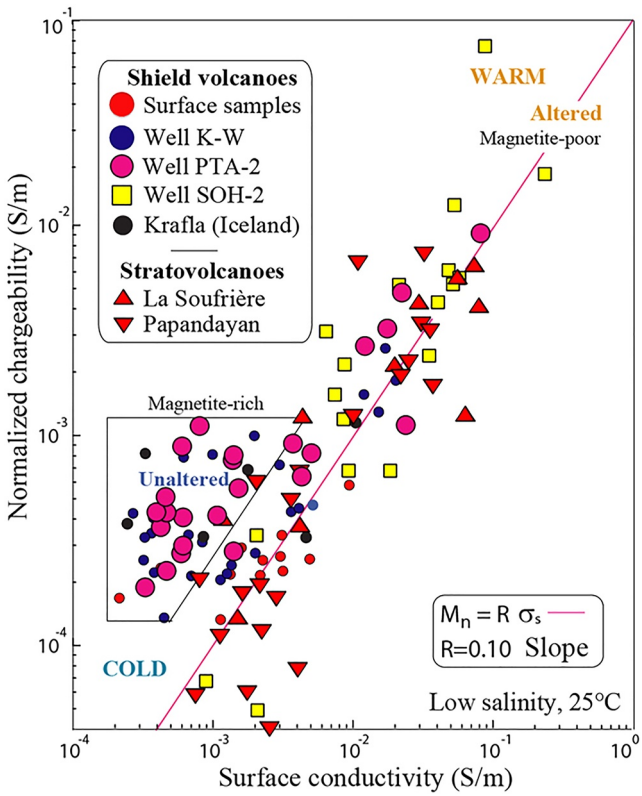

Figure 10. Results of the petrophysical investigations for the surface conductivity using volcanic rocks from both shield volcanoes and stratovolcanoes. Linear relationship between normalized chargeability (determined between 1 Hz and 1 kHz as the difference in the in-phase conductivity, low salinity, NaCl, 25°C) and the surface conductivity for the volcanic samples). The measured slope leads to the following value of the dimensionless number $R = 0.10$. Note that most of the samples located in the unaltered box of the figure have been collected at the ground surface or cored in shallow formations. The data from Krafla (Iceland) are from Revil, Qi, et al. (2018).

was done with a least-square technique penalizing roughness in the resulting tomograms. After 5 iterations, the RMS error reaches 23% for the impedance data and 5.0% for the apparent chargeability data. After inversion, the (intrinsic) normalized chargeability was obtained cell-by-cell by doing the product of the electrical conductivity σ and the chargeability M. An alternative definition of the chargeability is the ratio of the secondary voltage to the primary voltage. It can be obtained by integrating over time the first window of the secondary voltage decay curve (e.g., Mao & Revil, 2016). The results of the tomograms are displayed in Figure 9. The range of electrical conductivity data is grossly consistent with those obtained in the 3D conductivity tomogram.

4.2. Petrophysical Model

In the last decade, a lot of work has been done in understanding the induced polarization of volcanic rocks (see a review in Revil & Gresse, 2021, and references therein). In absence of semi-conductors (pyrite and magnetite), an expression of the normalized chargeability is given by Revil et al. (2017a, 2017b),

$$M_n = \frac{s_w^{n-1}}{F\phi}\rho_g \lambda\, \mathrm{CEC}, \tag{5}$$

$$M_n \approx \theta^{m-1}\rho_g \lambda\, \mathrm{CEC}, \tag{6}$$

where λ (in $m^2\ V^{-1}\ s^{-1}$) denotes the apparent mobility of the counterions for the polarization (Vinegar & Waxman, 1984). Equations 5 and 6 are valid in saturated and unsaturated conditions. The chargeability is defined as the ratio of the normalized chargeability by the conductivity, that is,

$$M = \frac{\theta^{m-1}\rho_g \lambda\, \mathrm{CEC}}{\theta^m \sigma_w(T) + \theta^{m-1}\rho_g B\mathrm{CEC}}. \tag{7}$$

Figure 10 shows that in absence of semi-conductors (pyrite and magnetite or titanomagnetite), the normalized chargeability M_n is proportional to the surface conductivity σ_S (compare Equation 3 with Equation 5). Whatever the temperature and the saturation in liquid water, the ratio between the two quantities is equal by the mobility ratio $\lambda/B = R$ defining the dimensionless number R. The broad range of experimental data shown in Figure 10 provides the value of the universal constant $R \approx 0.10 \pm 0.02$. In other words, the normalized chargeability and the surface conductivity are always proportional to each other in absence of semi-conductors.

In order to see if surface conductivity is the dominant conduction mechanisms or not, it is important to note that if the electrical conductivity is dominated by surface conductivity, we have (see Figure 10 and a detailed discussion in Revil et al., 2022, for stratovolcanoes)

$$M \equiv \frac{M_n}{\sigma_\infty} \rightarrow R \equiv \frac{\lambda}{B}, \tag{8}$$

where σ_∞ denotes the high-frequency conductivity (instantaneous conductivity), R is a dimensionless number defined as the ratio of the two mobilities λ and B (the quantity R is also the ratio between the normalized chargeability and the surface conductivity, see Figure 10). The key dimensionless number R is independent of the saturation and temperature of the porous material (Revil & Gresse, 2021). This result is very important since it means that induced polarization can be used to assess if surface conductivity is dominant or not in the conductivity tomogram of a volcano (Figure 11). In addition, since the dependence of the conductivity with the frequency is very small (less than 10%), we consider safely that $\sigma_\infty \approx \sigma(\theta,T)$ in Equation 1. Finally, the chargeability is obtained in the field by integrating the first window of the secondary voltage decay curve in time-domain induced polarization measurements (see Mao & Revil, 2016).

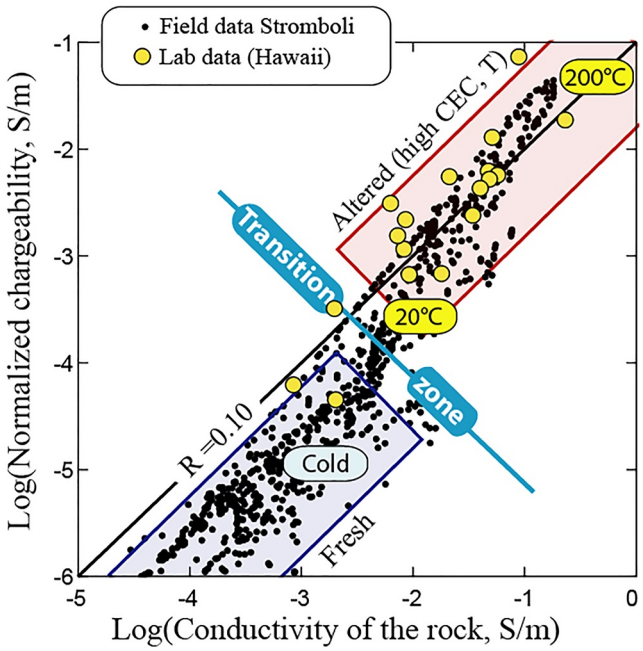

Figure 11. Relationship between the normalized chargeability and the electrical conductivity for the field data of Stromboli. When the data are close to the trend given by the dimensionless number $R = 0.10$, it means that the conductivity is dominated by its surface conductivity contribution, therefore by alteration. Altered rocks are associated with an electrical conductivity higher than 10^{-2} S m^{-1}. The laboratory data are from core samples from well SOH2 in Hawaii and represents the normalized chargeability versus the surface conductivity determined from conductivity data measured at different salinities. The temperatures are determined from the data shown in Figure 12.

5. Temperature Tomograms

We first check the relationship between the normalized chargeability and the electrical conductivity for the field data of Stromboli (Figure 11). As explained in the previous section, the ratio between these two quantities is close to the dimensionless number $R = 0.10$, it means that the conductivity is dominated by its surface conductivity contribution, therefore by alteration. When alteration dominates the conductivity response, the clay minerals with the higher cation exchange capacity (smectite) controls both the conductivity and normalized chargeability response of the volcanic rocks. Figure 12 shows that when this is the case, both conductivity and normalized chargeability depends directly on temperature for the entire stability domain of smectite (up to 220°C). This means that the production of smectite during the alteration process is a temperature-controlled process (see Revil et al., 2022).

The first relationship between the normalized chargeability and the temperature shown in Figure 12a was used to convert the normalized chargeability tomogram shown in Figure 9b into a temperature tomogram. The result presented in Figure 13 highlights cold and hot areas. Temperatures are not very high (~80°C), as already mentioned in previous works performed in the Pizzo area (Finizola et al., 2003, 2006; Revil et al., 2011). If compared with the 3D temperature tomogram obtained from the 3D conductivity distribution, we recover the same structure but the 2.5D inversion implies that the geometry remains the same in the strike direction, which limits the validity of the recovered amplitudes. This temperature range is typical from shallow hydrothermal fluid flows and the profile is located few tens of meters East of Pizzo coinciding with the P3 anomaly (see the orange star and dashed line in Figure 13 and "P3" in Figure 3c).

The tomogram is compared with soil CO_2 concentration data, subsurface temperature at 30 cm depth and self-potential data measured along the resistivity profile. The consistency between the data set is remarkable. The temperature and CO_2 peaks are aligned and coincide with the roots of the hottest temperature at depth (see the orange star and dashed line in Figure 13). The location of this anomaly matches the topographic boundary between the head of the Sciara del Fuoco and the Rina Grande sector collapses (see the orange star on Figure 13). This anomaly is consistent, at depth, with the gliding plane of Sciara del Fuoco and/or Rina Grande sector collapse, which is channeling the hydrothermal fluids up to the sub-surface through buoyancy. This interpretation is attested by the temperatures measured at 30 cm depth and CO_2 soil concentration data. About self-potential signal, the observed first-order change is not associated with the "P3" anomalies. Instead, it highlights a sharp self-potential gradient located at 1,200 m along the profile and associated with the boundary of NeoStromboli crater rim (blue star and blue dashed line on Figure 13), as already shown in previous works (Finizola et al., 2006; Revil et al., 2011, see also "NSt" crater boundary on Figure 4). It is also interesting to observe that a warm zone ($30 < T < 70$°C) is consistent with the PaleoStromboli III caldera boundary (see black star on Figure 13).

On a structural standpoint, the most striking result for the temperature tomogram deals with a vertical bifurcation of the hottest zone at depth. Considering the iso-temperature 80°C (corresponding to the more or less vertical thermal anomaly at depth), an inflexion point is located at about 600 m a.s.l. (see horizontal gray dashed line in Figure 13b). This deviation of the hot area (likely hot fluids) can be explained by a permeability heterogeneity, that is, a lithological and/or structural boundary, constraining rising hydrothermal fluids to change direction.

Moreover, it is important to note that the temperature tomogram (Figure 13b) is presented with a vertical exaggeration factor of 1.6. As a consequence, this change of direction is actually even more horizontal than what Figure 13b shows, and could be associated with the floor of the NeoStromboli crater. Indeed, previous works already evidence the NeoStromboli crater as a sealed zone impeding the rising of magmatic gases from depth (Finizola et al., 2002, 2006; Revil et al., 2011). This structural boundary at about 600 m a.s.l. is clear of first important for Stromboli volcano in terms of fluid migration. It is also important to note that the temperature

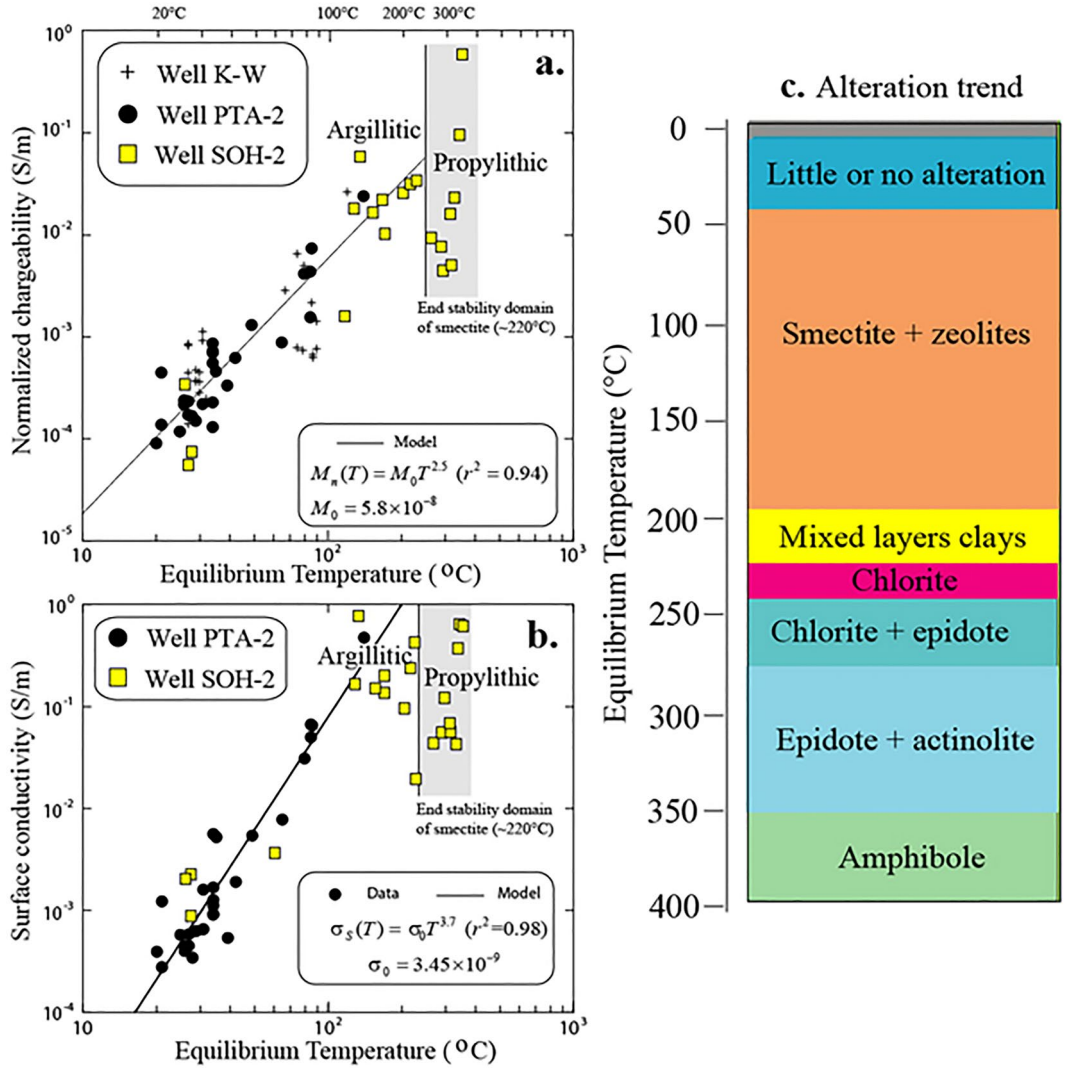

Figure 12. Relationship between either normalized chargeability or surface conductivity versus equilibrium temperature. (a) Normalized chargeability versus temperature. (b) Surface conductivity versus temperature. (c) Alteration trend with the equilibrium temperature for the secondary minerals (modified from Kousehlar et al., 2012).

obtained in this cross section is significantly lower with respect to the Figure 14 (from the 3D conductivity distribution). This lower temperature is due to the location of this profile crossing the summit of Stromboli, close to the Pizzo area, on the upper eastern flank, while the profile presented in Figure 14 cut the active crater area closer from heat sources. Recent works from Ripepe et al. (2021) and Sugimura et al. (2021) focusing on VLP signals evidenced seismic source locations a depth of 590 and 600 m a.s.l, respectively.

In the following part of this survey, we analyze 2D and 3D cross-sections cutting the active crater area. Our goal is to compare the temperature information at depth, obtained in this work with the seismicity location at Stromboli volcano, as well as volcano-tectonic events (Patané et al., 2017) and VLP events (Ripepe et al., 2021; Sugimura et al., 2021). In a second step, we use the surface conductivity/temperature relationship shown in Figure 12b to convert the 3D conductivity distribution into a temperature tomogram. The result is presented in Figure 14 assuming that electrical conductivity is dominated by surface conductivity (see Section 4). Along the section crossing Punta Lena—Vancori—the active crater area and San Vincenzo, we observe cold areas corresponding to the massive Vancori formation. A thermal plume can be observed in the central part of the edifice with temperatures around ~220–250°C.

Figure 15b displays a S-N cross-section of the entire Stromboli Island from Punta Lena, across Vancori, Fossetta, Fossa, Sciara del Fuoco, and up to Punta Labronzo. The direction of the profile (N8°E) was chosen to incorporate

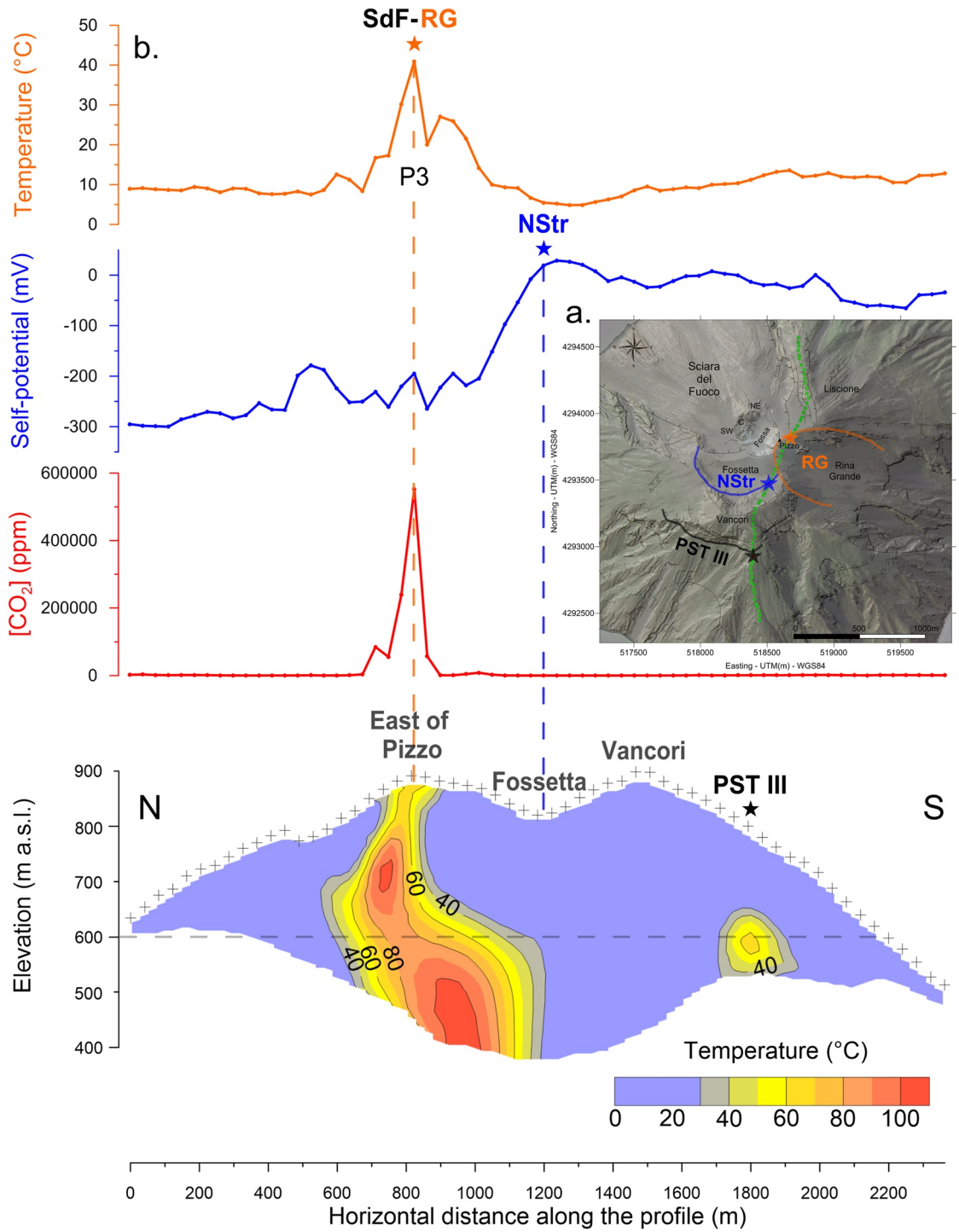

Figure 13. Interpretation of the data along the induced polarization profile. (a) Location (green dots) of the temperature tomogram. The orange, blue and black stars represent the anomalies visible along the profile. Other symbols: same as Figure 2. Note that the profile crosses at the East of Pizzo, and do not cross the Fossa area. (b) Temperature tomogram obtained from the normalized chargeability along the profile shown in Figure 9. The view is taken from the Sciara del Fuoco (vertical exaggeration 1.6). The temperature tomogram is associated with complementary field measurements; temperature at 30 cm depth, self-potential and soil CO_2 concentration. We use the transition zone boundary shown in Figure 11 to say that below a certain threshold, the volcanic rocks are cold. A clear temperature anomaly representing the uprising of hydrothermal fluids along at least two different structural boundaries can be identified in association with sub-surface temperature and CO_2 concentration peaks. SdF-RG stands for Sciara del Fuoco-Rina Grande boundary, NStr for NeoStromboli crater and PST III for PaleoStromboli III caldera. P3 is the thermal anomaly shown in Figure 3c.

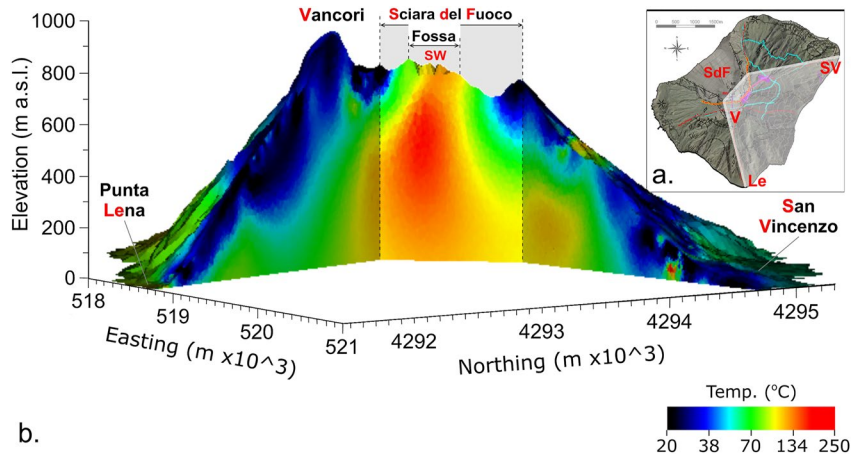

Figure 14. Temperature tomogram obtained at the scale of Stromboli from the electrical conductivity tomogram (see Figure 6). This is the first tomogram of temperature obtained on Stromboli volcano. (a) Position of the section crossing the Island of Stromboli. (b) Cross-section of the temperature obtained from the 3D conductivity tomogram.

the volcano-tectonic (VT) seismicity recorded along the same cross-section during the 2006–2007 periods (see black dots in Figure 15b from Patané et al., 2017).

The comparison between the model of temperature at depth with the measurements extracted from temperature at 30 cm depth (Figures 3b and 3c), self-potential (Figure 4) and CO_2 concentration (Figure 3e) maps underlines the importance of F3 and F6 anomalies located in the Fossa area. From a thermal point of view, the main heat source seems to be located below the SW crater. The importance of the SW crater in terms of observable seismic activity compared to the NE crater was also recently mentioned by seismologist working on the VLP source location (Ripepe et al., 2021; Sugimura et al., 2021). At lower altitude, the northernmost CO_2 anomaly is consistent with PaleoStromboli III caldera boundary while, to the south, the same structural boundary seems to be obstructed by the Vancori formation.

6. Comparison With Seismicity and Shallow Degassing

Based on the 3D temperature tomogram performed in this study, and using the seismological works recently published by Patané et al. (2017) for volcano-tectonic events and Ripepe et al. (2021) and Sugimura et al. (2021) for VLP source location, we can make inferences regarding both the hydrothermal body and the volcanic vents. The lateral extension of the main shallow volcano-tectonic seismicity located between 0 and 300 m a.s.l. matches with temperatures above 120°C (boundary between yellow and orange on Figure 15b). This volume underlines the main hydrothermal body highlighted as well by the seismicity in the first lower third of the aerial part of the volcanic edifice, and reveals a corresponding thermal lateral extension of about 600 m in diameter. It is very interesting to note that the highest temperature area (see red color in Figure 15b) is surrounded by but not associated with volcano-tectonic events. Considering that volcano-tectonic events are associated with rock fracturing, the red color area could represent the temperature transition inside Stromboli volcano from fragile to ductile material. In order to explain the sharp enlargement of the highest temperature area located between 300 and 600 m a.s.l., a shallow permanent magmatic reservoir centered at about 400–500 m a.s.l. below the SW crater could be hypothesized. This would represent the heat source feeding the hydrothermal system of Stromboli. The presence of such body would affect both the stability domain for smectite and the conductivity of the magma itself would need to be accounted for.

Other areas characterized by lower temperature (see green-light blue colors in Figure 15b) are also associated with hydrothermal fluids confined inside structural and lithological boundaries, such as the hydrothermal fluids sealed below the Fossetta/NeoStromboli crater area (see Finizola et al., 2006; Revil et al., 2011). The permeability of the NeoStromboli crater prevents hydrothermal fluids rising on its southern flank. On the opposite, the inner structure of PaleoStromboli III caldera allows the rising of hydrothermal fluids close to the surface on the northern flank, with preferential CO_2 degassing along this structural boundary (see Figures 15b and 15c and Finizola et al., 2002).

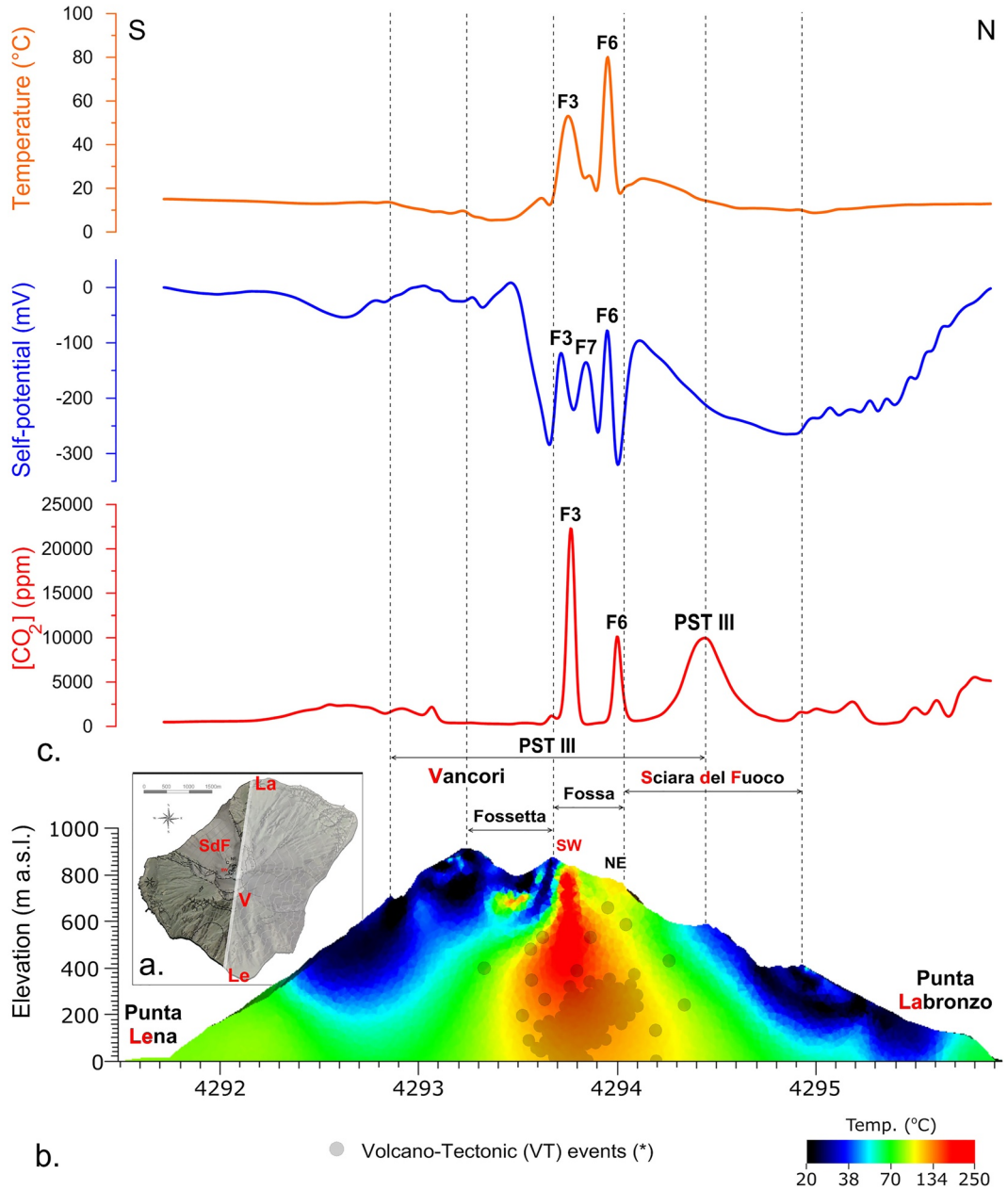

Figure 15. Temperature tomogram obtained at the scale of Stromboli from the electrical conductivity tomogram (see Figure 6). (a) Position of the profile along the island of Stromboli along N8°E direction. (b) Cross-section of the temperature tomogram. The gray-filled circles denote the position of the epicenters of local Volcano-Tectonic (VT) seismic events recorded during the 2006–2007 seismic experiment (Patanè et al., 2017). The local seismic events are related to rock fracturing mainly distributed below 300 m a.s.l. (c) Surface temperature, self-potential and soil CO_2 concentration along the profile.

In the Fossa area, two rising hydrothermal fluid systems can be located in the 3D tomogram in agreement with the position of the SW and NE active vents. The most striking result of the thermal model is the symmetric shape of the hottest body (red color in Figure 15b), beneath the SW crater.

Recent works focusing on VLP seismic sources show that the location of this seismic signal shifted ~100 m from the SW active crater toward the NW, and are located at ~600 m a.s.l. (Ripepe et al., 2021; Sugimura et al., 2021). The shallow VLP seismic signals at Stromboli volcano are clearly related with magmatic activity. Figure 16 presents a comparison between VLP source location (Ripepe et al., 2021; see blue star on Figure 16) and the temperature

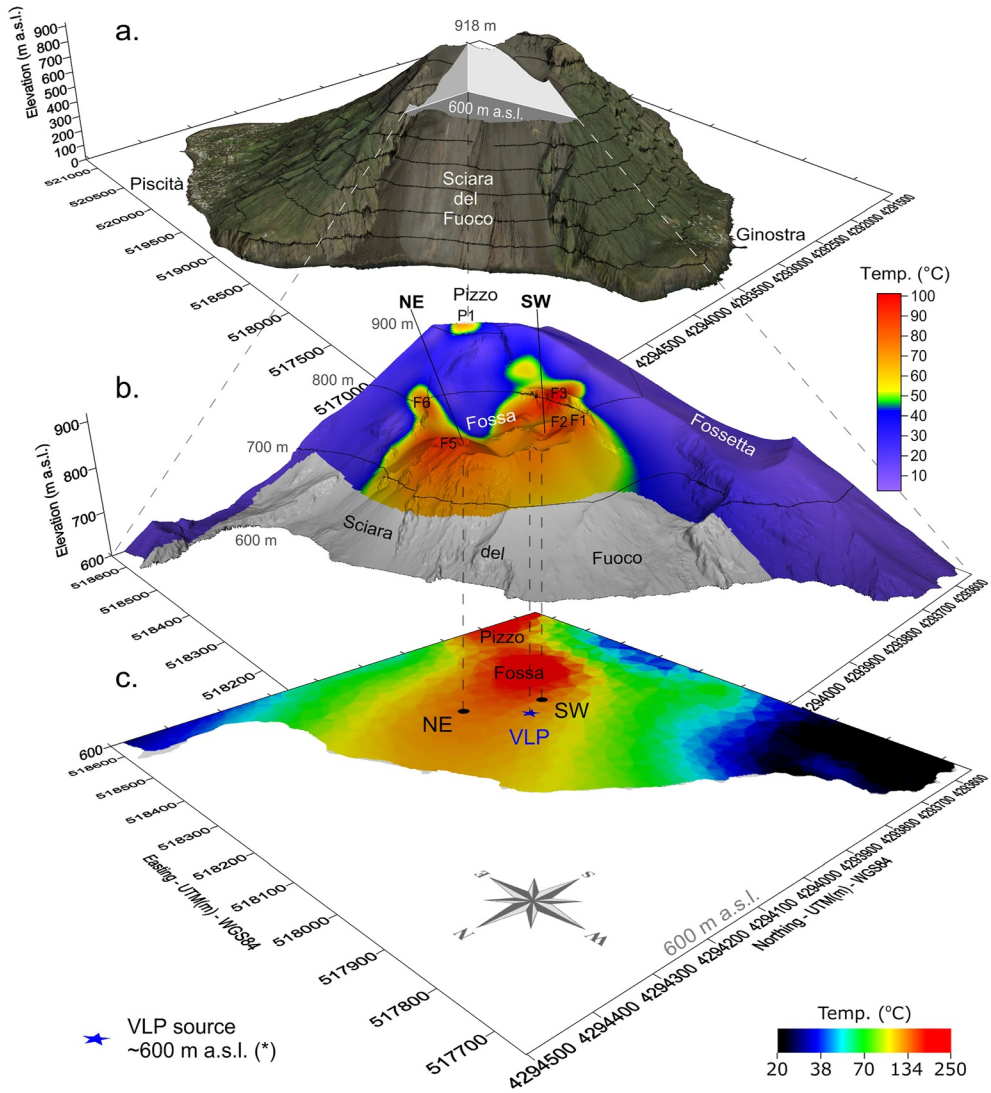

Figure 16. Comparison between temperature tomogram obtained at the scale of Stromboli, subsurface temperature at 30 cm depth and source of Very Long Period (VLP) seismic source associated with the permanent mild-eruptive Strombolian activity. NE and SW denote the two main active craters. (a) Orthophoto (22 May 2014) superimposed on a digital elevation model (DEM) of Stromboli showing the 3D block studied below. (b) Sub-surface temperature map measured at 30 cm depth superimposed on a DEM. (c) Temperature tomogram of Stromboli extracted on a horizontal plane at 600 m a.s.l., corresponding to the depth of VLP seismic signal. The blue star corresponds to the location of the source of the VLP seismic signal (Ripepe et al., 2021).

tomogram cut at 600 m a.s.l. on a horizontal plane. This figure evidences the VLP source bordering the highest temperature zone located below the Fossa (Figure 16c). The location of the heat source at 600 m a.s.l. is also in good agreement with the surface expression of the uprising hydrothermal fluids as shown by the F1, F2, F3, F5, and F6 thermal anomalies measured near the ground surface (Figure 16b). Figure 17 shows the highest temperature representing the upwelling of the hydrothermal fluids below the Pizzo crater area using the temperature tomogram with horizontal section cut each 10 m between 600 a.s.l. and 720 m a.s.l. The horizontal projection of the VLP seismic source is close to the boundary of the Pizzo crater fault (blue dots on Figure 17). The SW active crater is located at the boundary of the highest temperature area ($T > 100$°C), suggesting a nested structural boundary inside the Fossa area. This shallow geothermal reservoir is likely associated with an explosive/collapse event of an old crater, which has been refilled by permeable volcanic products such as scoria. The VLP signal underlines that the magma location at 600 m a.s.l. is influenced by the highest permeability area of the Pizzo crater fault at depth. The highest temperature area is probably influenced by more permeable products filling a small buried vent located inside the Pizzo

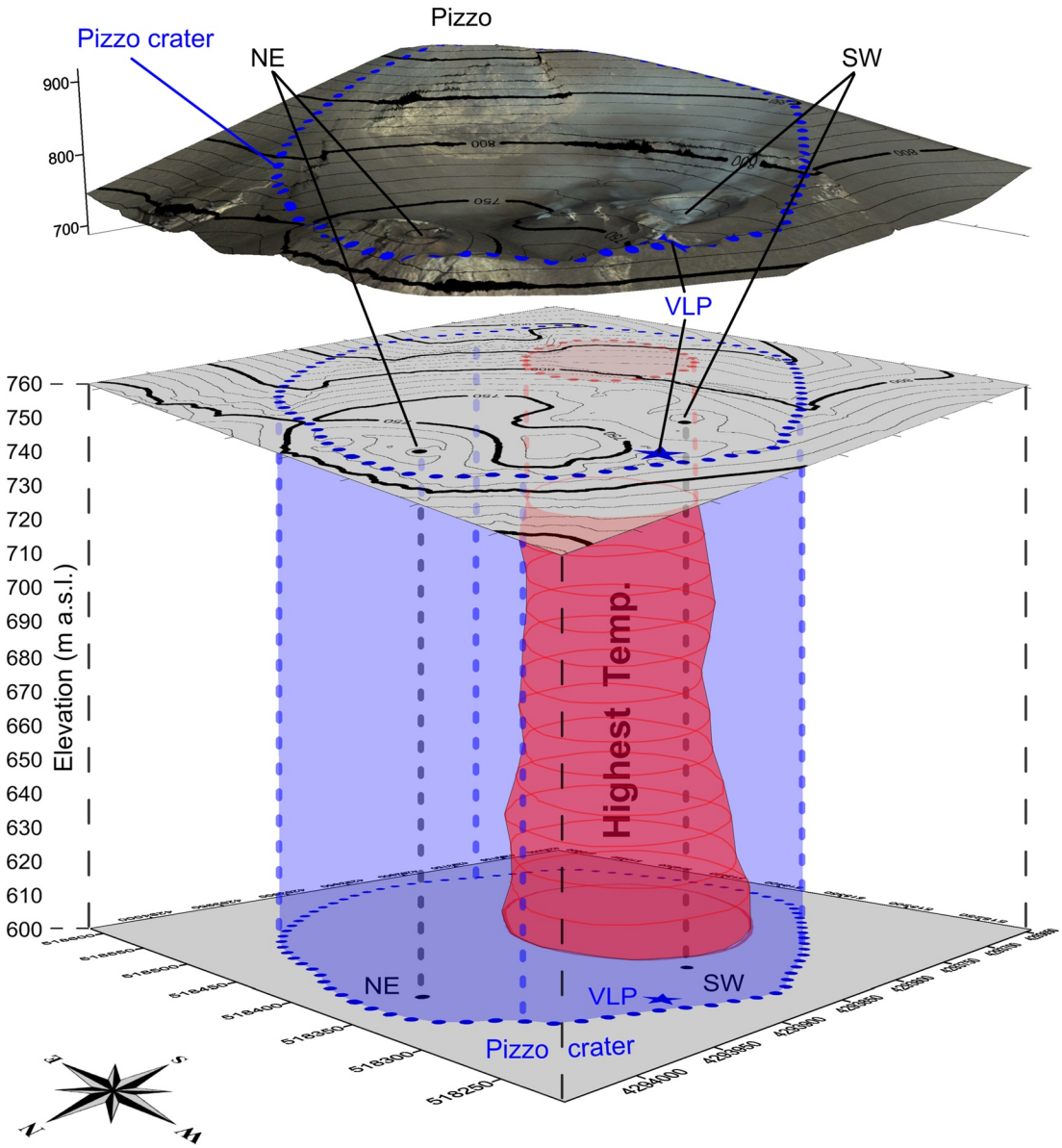

Figure 17. Upwelling of hydrothermal fluids in the Pizzo crater area. NE and SW denote the two main active craters. For each depth, we selected the areas above 100°C. The horizontal projection of the Very Long Period (VLP) seismic source and NE crater are located very close to the boundary of the Pizzo crater fault (blue dots). The area of hydrothermal fluids upwelling is distinct from the magmatic conduit and the VLP seismic source associated with it. The SW active crater is located close to the highest temperature area.

crater, in a sector where the Pizzo pyroclastic outcrops also disappear. This temperature distribution and hydrogeological feature could explain the explosive phreatomagmatic activity sometimes displayed by Stromboli volcano.

7. Concluding Statements

We have performed the first large-scale 3D conductivity and 2.5D induced polarization tomography at Stromboli volcano, an emblematic stratovolcano located in the Aeolian Islands, Italy. The ratio of the normalized chargeability to the conductivity indicates that high conductivity values are dominated by surface conductivity related to clay minerals produced by hydrothermal alteration of the volcanic rocks. In turn, this implies that the electrical conductivity tomogram can be used to assess the temperature distribution inside the volcano. A 3D temperature tomogram is produced from the conductivity tomogram showing the position of the highest temperature body in relation to the magmatic source and structural discontinuities.

This survey highlights a structural boundary at about 600 m a.s.l., that deviates the hydrothermal fluids, and that forces them into a narrow channel from the main deep thermal anomaly to the surface in the SW crater. We interpret this boundary as the floor of NeoStromboli crater. A secondary (weaker) channel seems to connect the main thermal anomaly to the NE crater. This would be in good accordance with the shift of the seismic activity from the SW crater to the NE crater during eruptions, as shown by the VLP signal migration. In the future, it would be interesting to add additional data using time-domain electromagnetic methods to increase the resolution of the tomograms and compare the temperature distribution to numerical simulation showing the thermal state of the volcano. The next step will be to jointly invert the electrical data with gravity data to analyze the electrical conductivity of the pore water.

Appendix A: Analysis of the Infrared Satellite Data

This appendix is related to the Figure 3d.

Two infrared radiance images were used: the long-wave infrared (TIR) band 10 (10.60–11.19 μm, 100-m spatial resolution, resampled to 30-m), and the short-wave infrared (SWIR) band 6 (1.57–1.65 μm, 30 m spatial resolution). Land surface temperature $t(\lambda)$ (K) was calculated, for each spectral radiance image, with the inverse Planck Function (Planck, 1900):

$$t(\lambda) = \frac{c_2}{\lambda \ln\left(1 + \frac{c_1 \lambda^{-5}}{R(\lambda)}\right)}, \tag{A1}$$

where $c_1 = 1.191042 \times 10^8$ (W · m^{-2} · sr^{-1} · μm^4) and $c_2 = 1.42387752 \times 10^4$ (K · μm) are two constants, and λ (μm) is the wavelength of the surface-emitted radiance $R(\lambda)$ (W · m^{-2} · sr^{-1} · μm^{-1}). To retrieve $R(\lambda)$, corrections of calibrated at-satellite radiance $R_{\text{in}}{}^*(\lambda)$ for atmospheric and emissivity effects were performed following the procedure developed by Harris (2013) for SWIR ands TIR (night-time) images, as follows:

$$R_{\text{SWIR}}(\lambda) = \frac{R_{\text{in}} * (\lambda) - R_{\text{noise}} * (\lambda)}{\tau(\lambda) s(\lambda)}, \tag{A2}$$

$$R_{\text{TIR}}(\lambda) = \frac{R_{\text{in}} * (\lambda) - R_U * (\lambda)}{\tau(\lambda) \varepsilon(\lambda)}, \tag{A3}$$

where, $R_{\text{noise}}{}^*(\lambda)$ is the estimated noise equal to 0.050 W m^{-2} sr^{-1} μm^{-1}, $R_U{}^*(\lambda)$ represents the atmosphere up-welling radiance, and $\tau(\lambda)$ is the atmospheric transmittance (dimensionless). $R_U{}^*(\lambda)$ and $\tau(\lambda)$ were calculated using the radiative transfer code MODTRAN (Berk et al., 1999) applying a model of mid-latitude winter atmosphere at an altitude of 0.3 km. Surface emissivity $\varepsilon(\lambda)$ (dimensionless) was retrieved using Sobrino et al. (1990) equation:

$$\varepsilon(\lambda) = \varepsilon_{v\lambda} P_v + \varepsilon_{s\lambda}(1 - P_v) + C_\lambda, \tag{A4}$$

where $\varepsilon_{v\lambda}$ and $\varepsilon_{s\lambda}$ correspond to emissivity values of bare soil and full vegetation pixels set at 0.880 and 0.990, respectively. The map of fractional vegetation cover P_v was determined through Carlson and Ripley (1997) formula, using the closest day time and cloud-free image from the infrared radiance images:

$$P_v = \left(\frac{\text{NDVI} - \text{NDVI}_\text{S}}{\text{NDVI}_\text{V} - \text{NDVI}_\text{S}}\right)^2, \tag{A5}$$

in which NDVI_S and NDVI_V are threshold values of the Normalized Difference Vegetation Index, defined for bare soil and vegetation at 0.2 and 0.5, respectively (Walawender et al., 2012). The index NDVI was calculated from Landsat-8 as:

$$\text{NDVI} = \frac{\text{band5} - \text{band4}}{\text{band5} + \text{band4}}. \tag{A6}$$

In Equation A4, the term C_λ corresponds to a surface roughness parameter, expressed as:

$$C_\lambda = (1 - \varepsilon_{v\lambda})\varepsilon_{s\lambda} + F'(1 - P_v), \tag{A7}$$

where F's a geometrical factor taken to a mean value of 0.55.

The dual band technique (Dozier, 1981) was implemented to solve the thermally mixed pixel, and thus retrieve the hot component of Stromboli vents. For that purpose, the dual band system equation was used according to:

$$R_{T_{\text{int},\lambda_1}} = f_{h,\lambda_1} R_{T_{h,\lambda_1}} + \left(1 - f_{h,\lambda_1}\right) R_{T_{C,\lambda_1}}, \tag{A8}$$

$$R_{T_{\text{int},\lambda_2}} = f_{h,\lambda_2} R_{T_{h,\lambda_2}} + \left(1 - f_{h,\lambda_2}\right) R_{T_{C,\lambda_2}}, \tag{A9}$$

where $R_{T_{h,\lambda_1}}$ and $R_{T_{\text{int},\lambda_2}}$ are the pixel-integrated surface-emitted radiance of band 6 and 10, respectively. $R_{T_{C,\lambda_1}}$ and $R_{T_{C,\lambda_2}}$ represent the calculated radiance from Equation A1, assuming the low-temperature surface T_C equal to 5°C (average surface temperature at ~600 m asl). f_{h,λ_1} and f_{h,λ_2} are the fraction of pixel of band 6 and 10, respectively, covering the high-temperature surface T_h. Finally, the solution T_h is obtained from Equations A8 and A9 when $f_{h,\lambda_1} / f_{h,\lambda_2} = 1$.

Data Availability Statement

The data are available at ZENODO (https://zenodo.org/, https://doi.org/10.5281/zenodo.7778490). The forward modeling and inversion code is available in open source at https://e4d.pnnl.gov.

Acknowledgments

The INSU-CNRS, the Istituto Nazionale di Geofisica e Vulcanologia (INGV), the Laboratoire GéoSciences Réunion-IPGP, and the DOE (Energy Efficiency and Renewable Energy, Geothermal Technologies Program, award DE-FG36-08GO018195) are thanked for funding this work. This study contributes to the IdEx Université de Paris ANR-18-IDEX-0001. We thank the personnel of the National Civil Protection and Mario Zaia (Zazà) for their continuous support. We thank Agnès Crespy, Barbara Suski, Casi Lock, Emilie Roulleau, Enzo Rizzo, Eve Tsang-Hin-Sun, Fabio Di Gangi, Fabrice Mourau, Geoffroy Avard, Gladys Le Masson, Guilhem Douillet, Jean Letort, Julie Albaric, Julie Morin, Julien Colonge, Laura Bennati, Laura Turinese, Maria Albo-Selma, Massimo Della Schiava, Matteo Lupi, Matteo Rossi, Nicole Wolyniec, Nicoló Praticelli, Philippe Menny, Pierre-Grégoire Scholl, Romain Boyer, Sabatino Piscitelli, Sandrine Poteaux, Sébastien Durand, Thibaut Bailly, Thierry Challan, Victor Villasante-Marcos, Virginie Meister, Xavier Rassion, Yashmin Chébli, and Aline Peltier, for their invaluable help in the field. M. Marsella is thanked for providing the high-resolution digital elevation model used in this paper. Special thanks to Denis Legrand for interesting discussion. Last but not the least, we thank the Editor, Michael Bostock, the Associate Editor, Max Moorkamp, and especially the two anonymous Referees for the amazing work done in helping us to deliver the best paper possible. This paper is dedicated to all the scientists who believe in hard work and passion.

References

Archie, G. E. (1942). The electrical resistivity log as an aid in determining some reservoir characteristics. *Transactions of the American Institute of Mining and Metallurgical Engineers*, *146*(01), 54–62. https://doi.org/10.2118/942054-G

Barberi, F., Civetta, L., Gasparini, P., Innocenti, F., Scandone, R., & Villari, L. (1974). Evolution of a section of the Africa-Europe plate boundary; paleomagnetic and volcanological evidence from Sicily. *Earth and Planetary Science Letters*, *22*(2), 123–132. https://doi.org/10.1016/0012-821X(74)90072-7

Barde-Cabusson, S., Finizola, A., & Grobbe, N. (2021). A practical approach for self-potential data acquisition, processing and visualization. *Interpretation*, *9*(1), T123–T143. https://doi.org/10.1190/INT-2020-0012.1

Berk, A., Anderson, G. P., Bernstein, L. S., Acharya, P. K., Dothe, H., Matthew, M. W., et al. (1999). *MODTRAN4 radiative transfer modeling for atmospheric correction, optical spectroscopic techniques and instrumentation for atmospheric and space research III*. International Society for Optics and Photonics. https://doi.org/10.1117/12.366388

Bolève, A., Janod, F., Revil, A., Lafon, A., & Fry, J.-J. (2011). Localization and quantification of leakages in dams using time-lapse self-potential measurements associated with salt tracer injection. *Journal of Hydrology*, *403*(3–4), 242–252. https://doi.org/10.1016/j.jhydrol.2011.04.008

Bonaccorso, A., Calvari, S., Garfì, G., Lodato, L., & Patanè, D. (2003). Dynamics of the December 2002 flank failure and tsunami at Stromboli volcano inferred by volcanological and geophysical observations. *Geophysical Research Letters*, *30*(18), 1941. https://doi.org/10.1029/2003GL017702

Bonasia, V., Luongo, G., & Montagna, S. (1973). A land gravity survey of the Aeolian Islands. *Bulletin of Volcanology*, *37*(1), 134–146. https://doi.org/10.1007/BF02596885

Bossolasco, M. (1943). La distribuzione del campomagnetico terrestre all'isola di Stromboli. *Geofisica Pura E Applicata*, *5*(1–2), 11–36. https://doi.org/10.1007/bf02000376

Calò, M., López Mazariegos, E. A., Tramelli, A., & Orazi, M. (2021). Hydrothermal systems characterization of the Stromboli volcano using spatial and temporal changes of the seismic velocities. *Journal of Volcanology and Geothermal Research*, *411*, 107177. https://doi.org/10.1016/j.jvolgeores.2021.107177

Carapezza, M. L., Ricci, T., Ranaldi, M., & Tarchini, L. (2009). Active degassing structures of Stromboli and variations in diffuse CO_2 output related to the volcanic activity. *Journal of Volcanology and Geothermal Research*, *182*(3–4), 231–245. https://doi.org/10.1016/j.jvolgeores.2008.08.006

Carlson, T. N., & Ripley, D. A. (1997). On the relation between NDVI, fractional vegetation cover, and leaf area index. *Remote Sensing of Environment*, *62*(3), 241–252. https://doi.org/10.1016/S0034-4257(97)00104-1

Casertano, L., & Pinna, E. (1971). La recente attività dello Stromboli (febbraio–marzo 1954). *Bollettino della Società Italiana Geofisica e Meteorologia*, *20*, 76–82.

Castellano, M., Augusti, V., De Cesare, W., Favali, P., Frugoni, F., Montuori, C., et al. (2008). Seismic tomography experiment at Italy's Stromboli volcano. *Eos, Transactions American Geophysical Union*, *89*(30), 269–270. https://doi.org/10.1029/2008EO300001

Chouet, B., Dawson, P., Ohminato, T., Martinit, M., Saccorotti, G., Giudicepietro, F., et al. (2003). Source mechanisms of explosions at Stromboli Volcano, Italy, determined from moment–tensor inversions of very-long-period data. *Journal of Geophysical Research*, *108*(B1), 2019. https://doi.org/10.1029/2002JB001919

Constable, S. C., Parker, R. L., & Constable, C. G. (1987). Occam's inversion: A practical algorithm for generating smooth models from electromagnetic sounding data. *Geophysics*, *52*(3), 289–300. https://doi.org/10.1190/1.1442303

Dozier, J. (1981). A method for satellite identification of surface temperature fields of subpixel resolution. *Remote Sensing of Environment*, *11*, 221–229. https://doi.org/10.1016/0034-4257(81)90021-3

Finizola, A., Aubert, M., Revil, A., Schütze, C., & Sortino, F. (2009). Importance of structural history in the summit area of Stromboli during the 2002–2003 eruptive crisis inferred from temperature, soil CO_2, self-potential, and electrical resistivity tomography. *Journal of Volcanology and Geothermal Research*, *183*(3–4), 213–227. https://doi.org/10.1016/j.jvolgeores.2009.04.002

Finizola, A., L´enat, J.-F., Macedo, O., Ramos, D., Thouret, J.-C., & Sortino, F. (2004). Fluid circulation and structural discontinuities inside Misti volcano (Peru) inferred from self-potential measurements. *Journal of Volcanology and Geothermal Research*, *135*(4), 343–360. https://doi.org/10.1016/j.jvolgeores.2004.03.009

Finizola, A., Revil, A., Rizzo, E., Piscitelli, S., Ricci, T., Morin, J., et al. (2006). Hydrogeological insights at Stromboli volcano (Italy) from geoelectrical, temperature, and CO_2 soil degassing investigations. *Geophysical Research Letters*, *33*(17), L17304. https://doi.org/10.1029/2006GL026842

Finizola, A., Ricci, T., Deiana, R., Barde Cabusson, S., Rossi, M., Praticelli, N., et al. (2010). Adventive hydrothermal circulation on Stromboli volcano (Aeolian Islands, Italy) revealed by geophysical and geochemical approaches: Implications for general fluid flow models on volcanoes. *Journal of Volcanology and Geothermal Research*, *196*(1–2), 111–119. https://doi.org/10.1016/j.jvolgeores.2010.07.022

Finizola, A., Sortino, S., Lénat, J.-F., Aubert, M., Ripepe, M., & Valenza, M. (2003). The summit hydrothermal system of Stromboli. New insights from self-potential, temperature, CO_2 and fumarolic fluid measurements. Structural and monitoring implications. *Bulletin of Volcanology*, *65*(7), 486–504. https://doi.org/10.1007/s00445-003-0276-z

Finizola, A., Sortino, S., Lénat, J.-F., & Valenza, M. (2002). Fluid circulation at Stromboli volcano (Aeolian Islands, Italy) from self-potential and CO_2 surveys. *Journal of Volcanology and Geothermal Research*, *116*(1–2), 1–18. https://doi.org/10.1016/S0377-0273(01)00327-4

Francalanci, L. (1987). Evoluzione vulcanologica e magmatologica diStromboli (Isole Eolie): Relazioni fra magmatismo calc-alcalino e shoshonitico. Ph D Thesis, Florence, Italy (p. 350).

Francalanci, L., Lucchi, F., Keller, J., De Astis, G., & Tranne, C. A. (2013). Eruptive, volcano-tectonic and magmatic history of the Stromboli volcano (north-eastern Aeolian archipelago). *Geological Society, London, Memoirs*, *37*(1), 397–471. https://doi.org/10.1144/M37.1

Gonzales, K., Finizola, A., Lénat, J.-F., Macedo, O., Ramos, D., Thouret, J.-C., et al. (2014). Asymmetrical structure, hydrothermal system and edifice stability: The case of Ubinas volcano, Peru, revealed by geophysical surveys. *Journal of Volcanology and Geothermal Research*, *276*, 132–144. https://doi.org/10.1016/j.jvolgeores.2014.02.020

Gresse, M., Uyeshima, M., Koyama, T., Hase, H., Aizawa, K., Yamaya, Y., et al. (2021). Hydrothermal and magmatic system of a volcanic island inferred from magnetotellurics, seismicity, self-potential, and thermal image: An example of Miyakejima (Japan). *Journal of Geophysical Research: Solid Earth*, *126*(6), e2021JB022034. https://doi.org/10.1016/e2021JB022034

Harris, A. (2013). *Thermal remote sensing of active volcanoes: A user's manual*. Cambridge University Press. https://doi.org/10.1017/CBO9781139029346

Hermans, T., Nguyen, F., Robert, T., & Revil, A. (2014). Geophysical methods for monitoring temperature changes in shallow low enthalpy geothermal systems. *Energies*, *7*(8), 5083–5118. https://doi.org/10.3390/en7085083

Hornig-Kjarsgaard, I., Keller, J., Koberski, U., Stadlbauer, E., Francalanci, L., & Lenhart, R. (1993). Geology, stratigraphy and volcanological evolution of the island of Stromboli, Aeolian arc, Italy. *Acta Vulcanologica*, *3*, 21–68.

Ishido, T. (2004). Electrokinetic mechanism for the "W"-shaped self-potential profile on volcanoes. *Geophysical Research Letters*, *31*(15), L15616. https://doi.org/10.1029/2004GL020409

Jardani, A., Revil, A., Barrash, W., Crespy, A., Rizzo, E., Straface, S., et al. (2009). Reconstruction of the water table from self-potential data: A Bayesian approach. *Groundwater*, *47*(2), 213–227. https://doi.org/10.1111/j.1745-6584.2008.00513.x

Johnson, T. C., Versteeg, R. J., Ward, A., Day-Lewis, F. D., & Revil, A. (2010). Improved hydrogeophysical characterization and monitoring through high performance electrical geophysical modeling and inversion. *Geophysics*, *75*(4), WA27–WA41. https://doi.org/10.1190/1.3475513

Keller, J., Hornig-Kjarsgaard, I., Koberski, U., Stadlbauer, E., & Lenhart, R. (1993). Geological map of the island of Stromboli. *Acta Vulcanologica*, *3*, 3.

Komori, K., Kagiyama, T., Hoshizumi, H., Takakura, S., & Mimura, M. (2010). Vertical mapping of hydrothermal fluids and alteration from bulk conductivity: Simple interpretation on the USDP-1 site, Unzen Volcano, SW Japan. *Journal of Volcanology and Geothermal Research*, *198*(3–4), 339–347. https://doi.org/10.1016/j.jvolgeores.2010.09.019

Kousehlar, M., Weisenberger, T. B., Tutti, F., & Mirnejad, H. (2012). Fluid control on low-temperature mineral formation in volcanic rocks of Kahrizak, Iran. *Geofluids*, *12*(4), 295–311. https://doi.org/10.1111/gfl.12001

Linde, N., Baron, L., Ricci, T., Finizola, A., Revil, A., Muccini, F., et al. (2014). 3-D density structure and geological evolution of Stromboli volcano (Aeolian Islands, Italy) inferred from land-based and sea-surface gravity data. *Journal of Volcanology and Geothermal Research*, *273*, 58–69. https://doi.org/10.1016/j.jvolgeores.2014.01.006

Linde, N., & Revil, A. (2007). A comment on "Electrical tomography of La Soufrière of Guadeloupe Volcano: Field experiments, 1D inversion and qualitative interpretation", by Nicollin, F. et al., (Earth Planet Sci. Lett. 244 (2006) 709–724). *Earth and Planetary Science Letters*, *258*(3–4), 619–622. https://doi.org/10.1016/j.epsl.2006.02.020

Mao, D., & Revil, A. (2016). Induced polarization response of porous media with metallic particles—Part 3. A new approach to time-domain induced polarization tomography. *Geophysics*, *81*(4), D345–D357. https://doi.org/10.1190/geo2015-0283.1

Marsella, M., Baldi, P., Coltelli, M., & Fabris, M. (2012). The morphological evolution of the Sciara del Fuoco since 1868: Reconstructing the effusive activity at Stromboli volcano. *Bulletin of Volcanology*, *74*(1), 231–248. https://doi.org/10.1007/s00445-011-0516-6

Okuma, S., Nakatsuka, T., Sugihara, M., Komazawa, M., Nakano, S., Furukawa, R., et al. (2003). Geophysical signature on the subsurface structure of the Aeolian Islands, Italy, IUGG 2003 Abstracts, Week B, B.256.

Okuma, S., Stotter, C., Supper, R., Nakatsuka, T., Furukawa, R., & Motschka, K. (2009). Aeromagnetic constraints on the subsurface structure of Stromboli Volcano, Aeolian Islands, Italy. *Tectonophysics*, *478*(1–2), 19–33. https://doi.org/10.1016/j.tecto.2009.02.035

Olhoeft, G. R. (1983). *Electrical properties of rocks and minerals*. Short Course Notes.

Olhoeft, G. R. (1985). Low-frequency electrical properties. *Geophysics*, *50*(12), 2492–2503. https://doi.org/10.1190/1.1441880

Pasquarè, G., Francalanci, L., Garduno, V. H., & Tibaldi, A. (1993). Structure and geologic evolution of the Stromboli volcano, Aeolian Islands, Italy. *Acta Vulcanologica*, *3*, 79–89.

Patanè, D., Barberi, G., De Gori, P., Cocina, O., Zuccarello, L., Garcia-Yeguas, A., et al. (2017). The shallow magma chamber of Stromboli Volcano (Italy). *Geophysical Research Letters*, *44*(13), 6589–6596. https://doi.org/10.1002/2017GL073008

Planck, M. (1900). Entropie und Temperatur strahlender Wärme. *Annals of Physics*, *306*(4), 719–737. https://doi.org/10.1002/andp.19003060410

Revil, A. (2013). Effective conductivity and permittivity of unsaturated porous materials in the frequency range 1 mHz–1 GHz. *Water Resources Research*, *49*, 306–327. https://doi.org/10.1029/2012WR012700

Revil, A., Cary, L., Fan, Q., Finizola, A., & Trolard, F. (2005). Self-potential signals associated with preferential ground water flow pathways in a buried paleo-channel. *Geophysical Research Letters*, *32*(7), L07401. https://doi.org/10.1029/2004GL022124

Revil, A., Coperey, A., Shao, Z., Florsch, N., Fabricius, I. L., Deng, Y., et al. (2017). Complex conductivity of soils. *Water Resources Research*, *53*(8), 7121–7147. https://doi.org/10.1002/2017WR020655

Revil, A., Finizola, A., Ricci, T., Delcher, E., Peltier, A., Barde-Cabusson, S., et al. (2011). Hydrogeology of Stromboli volcano, Aeolian Islands (Italy) from the interpretation of resistivity tomograms, self-potential, soil temperature, and soil CO_2 concentration measurements. *Geophysical Journal International*, *186*(3), 1078–1094. https://doi.org/10.1111/j.1365-246X.2011.05112.x

Revil, A., Finizola, A., Sortino, F., & Ripepe, M. (2004). Geophysical investigations at Stromboli volcano, Italy. Implications for ground water flow and paroxysmal activity. *Geophysical Journal International*, *157*(1), 426–440. https://doi.org/10.1111/j.1365-246X.2004.02181.x

Revil, A., Ghorbani, A., Gailler, L. S., Gresse, M., Panwar, N., & Sharma, R. (2018). Electrical conductivity and induced polarization investigations at Kilauea volcano, Hawai'i. *Journal of Volcanology and Geothermal Research*, *368*, 31–50. https://doi.org/10.1016/j.jvolgeores.2018.10.014

Revil, A., & Glover, P. W. J. (1998). Nature of surface electrical conductivity in natural sands, sandstones, and clays. *Geophysical Research Letters*, *25*(5), 691–694. https://doi.org/10.1029/98GL00296

Revil, A., & Gresse, M. (2021). Induced polarization as a tool to assess alteration in volcanic areas: A review. *Minerals*, *11*(9), 962. https://doi.org/10.3390/min11090962

Revil, A., Hermitte, D., Spangenberg, E., & Cochémé, J. J. (2002). Electrical properties of zeolitized volcaniclastic materials. *Journal of Geophysical Research*, *107*(B8), 2168. https://doi.org/10.1029/2001JB000599

Revil, A., Johnson, T. C., & Finizola, A. (2010). Three-dimensional resistivity tomography of Vulcan's forge, Vulcano Island, southern Italy. *Geophysical Research Letters*, *37*(15), L15308. https://doi.org/10.1029/2010GL043983

Revil, A., Le Breton, M., Niu, Q., Wallin, E., Haskins, E., & Thomas, D. M. (2017a). Induced polarization of volcanic rocks. 1. Surface versus quadrature conductivity. *Geophysical Journal International*, *208*(2), 826–844. https://doi.org/10.1093/gji/ggw444

Revil, A., Le Breton, M., Niu, Q., Wallin, E., Haskins, E., & Thomas, D. M. (2017b). Induced polarization of volcanic rocks. 2. Influence of pore size and permeability. *Geophysical Journal International*, *208*, 814–825. https://doi.org/10.1093/gji/ggw382

Revil, A., & Pezard, P. A. (1998). Streaming electrical potential anomaly along faults in geothermal areas. *Geophysical Research Letters*, *25*(16), 3197–3200. https://doi.org/10.1029/98GL02384

Revil, A., Qi, Y., Ghorbani, A., Soueid Ahmed, A., Ricci, T., & Labazuy, P. (2018). Electrical conductivity and induced polarization investigations at Krafla volcano, Iceland. *Journal of Volcanological and Geothermal Records*, *368*, 73–90. https://doi.org/10.1016/j.jvolgeores.2018.11.008

Revil, A., Qi, Y., Panwar, N., Gresse, M., Grandis, H., Sharma, R., et al. (2022). Induced polarization images alteration in stratovolcanoes. *Journal of Volcanology and Geothermal Research*, *429*, 107598. https://doi.org/10.1016/j.jvolgeores.2022.107598

Revil, A., Saracco, G., & Labazuy, P. (2003). The volcano-electric effect. *Journal of Geophysical Research*, *108*(B5), 2251. https://doi.org/10.1029/2002JB001835

Richards, K., Revil, A., Henderson, F., Batzle, M., & Haas, A. (2010). Pattern of shallow ground water flow at Mount Princeton Hot Springs, Colorado, using geoelectrical methods. *Journal of Volcanology and Geothermal Research*, *198*(1–2), 217–232. https://doi.org/10.1016/j.jvolgeores.2010.09.001

Ripepe, M., Delle Donne, D., Legrand, D., Valade, S., & Lacanna, G. (2021). Magma pressure discharge induces very long period seismicity. *Scientific Reports*, *11*(1), 20065. https://doi.org/10.1038/s41598-021-99513-4

Romagnoli, C., Casalbore, D., Chiocci, F. L., & Bosman, A. (2009). Offshore evidence of large-scale lateral collapses on the eastern flank of Stromboli, Italy, due to structurally-controlled, bilateral flank instability. *Marine Geology*, *262*(1–4), 1–13. https://doi.org/10.1016/j.margeo.2009.02.004

Rosi, M. (1980). The island of Stromboli. *Rendiconti della Societ Italiana di Mineralogia e Petrologia*, *36*, 345–368.

Rücker, C., Günther, T., & Spitzer, K. (2006). Three-dimensional modelling and inversion of DC resistivity data incorporating topography-I. Modelling. *Geophysical Journal International*, *166*(2), 495–505. https://doi.org/10.1111/j.1365-246X.2006.03010.x

Sinclair, A. J. (1974). Selection of threshold values in geochemical data using probability graphs. *Journal of Geochemical Exploration*, *3*(2), 129–149. https://doi.org/10.1016/0375-6742(74)90030-2

Sobrino, J. A., Caselles, V., & Becker, F. (1990). Significance of the remotely sensed thermal infrared measurements obtained over a citrus orchard. *ISPRS Journal of Photogrammetry and Remote Sensing*, *44*(6), 343–354. https://doi.org/10.1016/0924-2716(90)90077-O

Soueid Ahmed, A., Revil, A., Byrdina, S., Coperey, A., Gailler, L., Grobbe, N., et al. (2018). 3D electrical conductivity tomography of volcanoes, Journal of. *Volcanological and Geothermal Records*, *356*, 243–263. https://doi.org/10.1016/j.jvolgeores.2018.03.017

Sugimura, S., Nishimura, T., Lacanna, G., Legrand, D., Valade, S., & Ripepe, M. (2021). Seismic source migration during Strombolian eruptions inferred by very near-field broadband seismic network. *Journal of Geophysical Research: Solid Earth*, *126*(12), e2021JB022623. https://doi.org/10.1029/2021JB022623

Tarquini, S., Isola, I., Favalli, M., & Battistini, A. (2007). TINITALY, a digital elevation model of Italy with a 10 meters cell size, Istituto Nazionale di Geofisica e Vulcanologia (INGV), Italy. https://doi.org/10.13127/TINITALY/1.0

Tioukov, V., Alexandrov, A., Bozza, C., Consiglio, L., D'Ambrosio, N., De Lellis, G., et al. (2019). First muography of Stromboli volcano. *Scientific Reports*, *9*(1), 6695. https://doi.org/10.1038/s41598-019-43131-8

Titov, K., Revil, A., Konasovsky, P., Straface, S., & Troisi, S. (2005). Numerical modeling of self-potential signals associated with a pumping test experiment. *Geophysical Journal International*, *162*(2), 641–650. https://doi.org/10.1111/j.1365-246x.2005.02676.x

Villasante-Marcos, V., Finizola, A., Abella, R., Barde-Cabusson, S., Blanco, M. J., Brenes, B., et al. (2014). Hydrothermal system of Central Tenerife volcanic complex, Canary islands (Spain), inferred from self-potential measurements. *Journal of Volcanology and Geothermal Research*, *272*, 59–77. https://doi.org/10.1016/j.jvolgeores.2013.12.007

Vinegar, H., & Waxman, M. (1984). Induced polarization of shaly sands. *Geophysics*, *49*(8), 1267–1287. https://doi.org/10.1190/1.1441755

Walawender, J., Hajto, M., & Iwaniuk, P. (2012). A new ArcGIS toolset for automated mapping of land surface temperature with the use of LANDSAT satellite data (pp. 4371–4374). https://doi.org/10.1109/IGARSS.2012.6350405

Waxman, M. H., & Smits, L. J. M. (1968). Electrical conductivities in oil bearing shaly sands. *Society of Petroleum Engineers Journal*, *8*(02), 107–122. https://doi.org/10.2118/1863-A

Yokoyama, I. (1959). Sulla distribuzione del campo geomagnetico all'isola di Stromboli. *Bollettino della Società Italiana Geofisica e Meteorologia*, *7*, 53–56.